



NTNU – Trondheim
Norwegian University of
Science and Technology

Development of Hydrophobic Surfaces for Anti-Icing Applications

Steel Substrates

Ole-Bjørn Ellingsen Moe

Materials Science and Engineering

Submission date: June 2015

Supervisor: Hilde Lea Lein, IMTE

Co-supervisor: Sidsel Meli Hanetho, SINTEF
Christian Simon, SINTEF
Per Stenstad, SINTEF

Norwegian University of Science and Technology
Department of Materials Science and Engineering

Acknowledgements

Before we proceed to the more academical part of this thesis, I would like to express my appreciation for getting the opportunity to work within the field of hydrophobicity and anti-icing. This field has proven to be most interesting, both its theory and potential.

The people deserving special gratitude are my supervisor Hilde Lea Lein and co-supervisor Sidsel Meli Hanetho. Throughout the year I have worked with you, you have shown a keen interest in my work and motivated me to not only work hard but also to appreciate it. The open door policy, the low threshold for discussion, and weekly meetings are something every student values highly. Raymond Luneng and Vegard Hornnes, two other students working with Hilde and Sidsel, also deserve gratitude and appreciation for cooperation and good atmosphere whilst working.

Furthermore, I would like to thank co-supervisors Christian Simon and Per Stenstad for the suggestions and insight shown in our meeting, Yingda Yu for the SEM training, Zhiliang Zhang for valuable knowledge shared regarding hydrophobicity, Mari-Ann Einarsrud for suggestions regarding the synthesis of ZnO-nanowires, the people at NanoLab, the Battery research group, and the people at K2 for the good atmosphere, willingness to help, and interest shown.

The last thank you goes out to my classmates with whom I have shared office, and with whom I now end a five year educational journey. The good atmosphere has made it easy to work long hours.

Preface

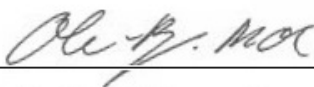
This master's thesis is written during the spring of 2015, the last semester of my master's degree in Material's Science and Engineering at the Norwegian University of Science and Technology (NTNU). The work was performed at the Department of Materials Technology (IMT), more specifically at the Inorganic Materials and Ceramics Research group, with associate professor Hilde Lea Lein as my supervisor.

SINTEF Materials and Energy has supported the project, where Sidsel Meli Hanetho, Christian Simon and Per Stenstad have been co-supervisors.

During the project the author has cooperated with Raymond Luneng and Vegard Hornnes, two other master students who studied the relationship between hydrophobicity and icing behaviour. Raymond focused on introducing roughness through SiO₂-spheres within the coating material, whereas Vegard focused on the mechanical properties of the coating.

The experimental work was mainly performed by the author. The viscosity measurement and the SEM-imaging of the sol were performed by Raymond.

Trondheim, June 11, 2015



Ole-Bjørn Ellingsen Moe

Abstract

Icing is a major problem for ships, airplanes, and wind turbines, among many other applications. To reduce or remove icing is extremely costly and is constantly in need of manpower. In this thesis the possibility of a passive resolution is investigated; a surface that reduces icing without external influence. A hydrophobic surface on steel is first developed through modification of topography and subsequent coating. Further, the icing behaviour of these hydrophobic surfaces are investigated.

The surface modification was performed by creating a hierarchical surface roughness by sand blasting and subsequent synthesis of ZnO-nanowires, a combination not found similar in literature. Samples with solely micrometric and nanometric roughness were also created in order to compare with the hierarchical roughness. Deposition of a highly hydrophobic coating layer was performed by dip-coating and vapour deposition.

When nanometric roughness was induced, dip-coating was no longer an applicable method of deposition, as the coating layer was too thick and compromised the topography. Vapour deposition had no such negative effects on the topography, which resulted in superior contact angle values.

Superhydrophobic contact angle values ($> 150^\circ$) were achieved for all samples where roughness was induced. The superior hydrophobic behaviour was observed on the sample with hierarchical roughness, with a contact angle of $164^\circ \pm 1.54^\circ$. Upon measuring the contact angle hysteresis, superhydrophobic behaviour was not observed. The hierarchical sample showed a hysteresis value of approximately 80° . The sample with superior hysteresis values was the sand blasted sample, with a value of 37° . These values suggest poor performance regarding icephobicity, as hysteresis values near zero are desired.

During the icing experiments, all samples showed the same behaviour with no definite prevention of crystallisation. Upon deicing the ice melted and slid off of all samples within 6 minutes, except the hierarchical sample where the water seemed to adhere more strongly, leaving the sample wet for a longer period of time.

These observations lead to the hypothesis that the ZnO-nanowires promote an undesirable state of wetting, Wenzel wetting, which would increase the adhesion of water significantly, causing large hysteresis values and no slide-off behaviour. The hysteresis value measured on the sand blasted sample was however also too high.

This may be due to misalignments of the hydrophobic molecules deposited on the surface.

In order to achieve hydrophobic surfaces with anti-icing properties, the sole development of hierarchical roughness is thus not enough. The dimensions of both the micrometric and nanometric structures must be within the range of achieving the desired Cassie-Baxter wetting state, and resist a subsequent transition to the Wenzel state. This may be achieved by an increase in ZnO-nanowire density and height, along with a decrease of the diameters. In addition, the coating needs investigation to ensure the correct alignment of the hydrophobic molecules.

Sammendrag

Ising er et stort og kostbart problem i flyindustrien, for båter, vindmøller og mange andre områder. Metodene som brukes for å fjerne isen er i tillegg ikke-miljøvennlige og trenger aktiv arbeidskraft. I denne oppgaven undersøkes potensialet til vann-avstøtende overflater til også å frastøte og hindre ising. Målet er å danne en overflate som minimerer adhesjonen og dannelsen av is, i den grad at vind eller tyngdekraft kan fjerne isen, eller eventuelt vannet før ising skjer. Dette gjøres gjennom å konstruere en hierarkisk ru overflate, for så å deponere en vannavstøtende coating på overflaten.

I denne oppgaven ble ruheten dannet ved å kombinere sandblåsing og syntese av ZnO-nanotråder, en kombinasjon ikke funnet tilsvarende i litteraturen. Prøver behandlet kun med sandblåsing eller syntese av ZnO-nanotråder ble også laget for sammenligning. Deponering av en vannavstøtende coating ble til slutt gjennomført ved hjelp av "dip-coating" og "vapour deposition".

For prøver med nanostruktur var ikke lenger "dip-coating" en nøyaktig nok metode. Det deponerte laget ble for tykt, noe som resulterte i ødelagt topografi. "Vapour deposition" hadde ingen slik negativ effekt, noe som resulterte i bedre kontaktvinkelmålinger.

Superhydrofobe kontaktvinkler ($> 150^\circ$) ble målt på alle prøver hvor ruhet ble introdusert. Høyest kontaktvinkler ble målt på prøven med hierarkisk ruhet, med $164^\circ \pm 1.54^\circ$. Ved måling av hysteresen ble derimot superhydrofobe verdier ikke observert. Den hierarkiske prøven målte en hysteresen på 80° , mens den laveste verdien var 37° for den sandblåste prøven. Disse verdiene ville sannsynligvis resultere i dårlig anti-ising egenskaper, der en hystereseverdi nærme null er ønskelig.

Ingen prøver viste definitive anti-isingsegenskaper under testing. Under de-ising av prøvene ble det derimot observert at isen på alle prøver smeltet og skled av iløpet av 6 minutter, utenom på den hierarkiske prøven hvor isen smeltet, men aldri skled av.

Høy hystereseverdier og vannet som aldri skled av resulterte i to hypoteser. Den ene er en ugunstig fuktingsopptak, Wenzel-fukting, når ZnO-nanotråder er på overflaten. Hysteresen målt på kun-sandblåste prøver er derimot også for høy, noe som leder til hypotesen om at de hydrofobe molekylene på overflaten kan være orientert ugunstig.

For å danne overflater som frastøter is er altså ikke en hierarkisk struktur nok. Dimensjonene til både mikro- og nanostrukturen må være i et område som resulterer i Cassie-Baxter fukting, samtidig som en potensiell Wenzel-overgang blir hindret. Dette kan gjennomføres ved å bedre tetthet, høyde og diameter på nanotrådene. I tillegg må coatingen undersøkes for å verifisere orienteringen til de hydrofobe molekylene.

Contents

Acknowledgements	i
Preface	iii
Abstract	v
Sammendrag	vii
List of Figures	xi
List of Tables	xiii
1 Introduction	1
1.1 Background	1
1.2 Aim of Work	3
2 Theory	5
2.1 Wetting	5
2.1.1 Superhydrophobic Surfaces	6
2.1.2 Contact Angle Hysteresis	8
2.1.3 Icephobicity	11
2.1.4 The Hydrophobicity-Icephobicity Relationship	12
2.1.5 Characterisation of Wetting Behaviour	14
2.2 Stainless Steel	16
2.3 Inducing Roughness	17
2.3.1 Micrometric Roughness	17
2.3.2 Nanometric Roughness	18
2.3.3 Surface Characterisation	23
2.4 Sol-Gel Synthesis	24
2.4.1 Overview	24
2.4.2 Synthesis	25
2.5 Deposition	29
2.5.1 Dip-Coating	29
2.5.2 Vapour Deposition	32

3	Experimental	35
3.1	Inducing Roughness	36
3.1.1	Micrometric Roughness	36
3.1.2	Nanometric Roughness	36
3.1.3	Surface Characterisation	40
3.2	Synthesis of Solution	41
3.2.1	Chemicals and Sol Parameters	41
3.2.2	Synthesis Procedure	42
3.2.3	Sol Characterisation	43
3.3	Deposition	44
3.4	Wetting Characteristics	46
3.4.1	Water Contact Angle	46
3.4.2	Hysteresis	46
3.5	Icing Characteristics	48
4	Results	51
4.1	Surface Roughness Characterisation	51
4.1.1	Surface Morphology of Sand Blasted Samples	52
4.1.2	Surface Morphology of Samples with ZnO-Nanowires	53
4.1.3	Surface Morphology of Samples with Hierarchical Structure	53
4.2	Sol Characterisation	54
4.3	Coating and Wetting Characterisation	55
4.3.1	Surface Morphology after Coating	55
4.3.2	Wetting Characterisation	56
4.4	Icing Behaviour	59
5	Discussion	63
5.1	Surface Treatments Pre-Coating	63
5.1.1	Sand Blasting	63
5.1.2	ZnO-Nanowire Synthesis	64
5.2	Deposition	64
5.2.1	Dip-Coating	64
5.2.2	Vapour Deposition	65
5.2.3	The Importance of Ethanol-Rinsing	65
5.3	Wetting	66
5.4	Anti-Icing Results	69
5.5	Summary of Discussion	70
6	Conclusion	71
7	Further Work	73
	References	75
	Appendices	A1
A	Stoichiometric to Volumetric Calculations	A1

List of Figures

1.1	A plane wing and windmill in need of deicing.	1
2.1	The wetting of a droplet with low and high interfacial energy.	5
2.2	How interfacial energies affect the wetting of a surface	6
2.3	Surface structure of the Lotus leaf	7
2.4	Three different main wetting behaviours	8
2.5	A method for measuring contact angle hysteresis by inclination.	9
2.6	The effect of a retained air-layer on drag.	9
2.7	Cassie Impregnating state of wetting.	10
2.8	Four wetting states dependent on the structure's peak-to-peak distances.	10
2.9	The probability of icing on a surface as a function of particle size	12
2.10	Ice adhesion strength as a function of contact angle hysteresis and receding contact angle	13
2.11	A typical optical tensiometer for wetting measurements.	14
2.12	A method for measuring the contact angle hysteresis by extraction and injection of water.	15
2.13	Corrosion protection from chromium oxide on a steel surface	16
2.14	Abrasive blasting.	18
2.15	Surfaces with nano-structured features by a bottom-up approach.	18
2.16	A hierarchical surface roughness made by laser.	19
2.17	Seed-layer of heat-treated zinc acetate.	20
2.18	How ZnO is grown dependent on initial solution pH	22
2.19	The principle of a stylus profilometer	23
2.20	Possible products through the sol-gel method.	24
2.21	The molecular structure of a highly used silane for sol-gel purposes, and its ternary phase diagram with water and alcohol.	25
2.22	How pH affects the rate of the hydrolysis and condensation reactions	26
2.23	The hydrolysis and condensation reactions depending on acid- or base catalysis.	26
2.24	Gelation of a sol, from small particles to one single gel	27
2.25	How pH affects growth and gelation of sols, and the resulting coating.	28
2.26	The dip-coating procedure	30
2.27	The bonding reaction between alkoxysilanes and OH-groups.	31

2.28	The behaviour of a newtonian fluid	31
2.29	The Chemical Vapour Deposition process.	32
2.30	The structure of the β -silane.	33
2.31	The bonding reaction between the β -silane and OH-groups.	34
3.1	The experimental work performed in this thesis	35
3.2	The sand blasting cabinet used to induce micrometric roughness.	36
3.3	The oven and placements of the substrates inside the oven during heat-treatment.	38
3.4	Autoclave and sample holder used during ZnO-wire synthesis	38
3.5	The placement of the autoclave inside the oven during growth of ZnO-nanowires.	39
3.6	The Veeco Dektak 150 profilometer.	40
3.7	Molecular structure of the β -silane	41
3.8	The experimental setup of the sol-gel synthesis	42
3.9	Haake RheoWin Mars III rotational rheometer from Thermo Scientific.	43
3.10	The dip-coating equipment	44
3.11	Experimental setup when vapour depositing.	45
3.12	The heating-plate on which the samples were treated after vapour deposition.	45
3.13	The Attension Theta T330 optical tensiometer from Biolin Scientific.	46
3.14	Placement of the tip of the pipette during hysteresis measurements	47
3.15	The single-droplet icing experimental setup.	48
3.16	The spray-icing experimental setup.	49
4.1	SEM-image of an as-delivered steel surface	51
4.2	SEM-image and topography of a sand blasted sample.	52
4.3	SEM-images of smooth surfaces with ZnO-nanowires	53
4.4	SEM-images of sand blasted surfaces with ZnO-nanowires	53
4.5	Particles in the sol.	54
4.6	The effect of dip-coating and vapour deposition on the nano-structure.	55
4.7	The effect of ethanol rinsing on contact angle values.	56
4.8	High adhesion between droplet and surface.	57
4.9	A droplet when ascending and receding contact angle was measured.	58
4.10	Low adhesion between the droplet and the surface, resulting in difficulties when depositing the droplet.	59
4.11	The droplet when ascending and receding contact angle value was measured on the hierarchical structured sample, after forcing of the droplet onto the surface.	59
4.12	Single droplet test results.	60
4.13	Results from the spray-icing and deicing of the vapour deposited samples.	61
4.14	Small unfrozen droplet during spray-icing test.	61

List of Tables

2.1	The diameter, density and length of ZnO nanorods corresponding to the thickness of the seed layer.	21
2.2	An overview of the equipment used for surface characterisation.	23
3.1	The chemicals used during the synthesis of ZnO-nanowires	37
3.2	The parameters used during roughness measurements of sand blasted samples.	40
3.3	The sol recipe.	41
3.4	Chemicals used during sol-gel synthesis	41
3.5	Parameters used during viscosity measurements of the sol.	43
3.6	The parameters used during dip-coating.	44
4.1	R_a -value and peak-to-peak distance of the sand blasted samples.	52
4.2	The viscosity of the sol.	54
4.3	An overview over the abbreviations used for the different samples.	55
4.4	Average contact angles for the different samples	56
4.5	Hysteresis values of the vapour deposited samples.	58
A1	Molar weight and density of β -silane, ethanol, and deionized-water.	A1

Chapter 1

Introduction

1.1 Background

Icing is a major problem for ships, airplanes, wind turbines, heat exchangers, and many other applications [1]. A lot of resources are constantly used to reduce or remove ice, and the methods used are mostly expensive, inefficient, in need of manpower, or even non-environmental. The United States Environmental Protection Agency reported in 2009 that in the years 2002 to 2005, over 75 billion litres of glycol was used annually for deicing airplanes in the US alone [2]. When companies, such as privatefly.com, offer deicing with glycol for €5 a litre [3], one can understand that deicing is costly. Even though the efforts made to remove the ice are huge, the icing still causes problems. Scientific American writes that icing on planes has been a contributing factor to 9.5 percent of fatal air carriers accidents [4]. The development of ice on plane wings and tails will roughen the smooth surface, as shown in Figure 1.1(a), and cause drag and less lifting force, causing the plane to become harder to manoeuvre [4, 5].



Figure 1.1: (a) Plane wing and (b) windmill in need of deicing [5, 6].

Another example is the icing on wind turbines, mentioned by Teknisk Ukeblad [6]. When fog or low-hanging clouds surround the turbines, icing will occur as shown in Figure 1.1(b). This will in turn lead to a lower energy production or even a complete stop of the turbines. A new solution to this problem is to use a helicopter to spray warm water on the turbines [6]. Although this method is effective compared to older methods, it is clear that the cost is still high, the method time consuming, and manpower is still needed.

Nowadays, as the oil industry moves towards more arctic climates, anti-icing is becoming more important than ever. As the oil rigs travel further, so does more ships and vessels, which are constantly subjected to phenomenas like sea spray icing. In the worst case scenario, sea spray icing may lead to accumulation of ice on the boat in a degree that affects the stability, and may even cause the ship to sink [7].

With these examples in mind, finding inexpensive and environmentally friendly methods to remove ice is important, not only for saving money but potentially lives. The tendency is also clearly visible in the literature where more and more papers about anti-icing are being published, especially within surface science. The main goal of several of these papers is to develop a passive resolution, a surface, that removes water and ice without direct influence from external chemicals or manpower. One theory is that this surface needs to have a low water and ice adhesion, causing ice to easily be removed, and repel water before it freezes. Although surfaces possessing some of these properties are already developed, there are many challenges yet to conquer, one being the icephobicity and hydrophobicity relationship, which is not well understood. Many scientists believe there is a direct correlation between the two properties, some believe there are none, while others believe the correlations only exist in given conditions. For the surface to withstand use on ships and airplanes, the coating also needs good mechanical properties which has shown to be a challenge. The possibilities and potential of these anti-icing surfaces are enormous and the challenges big.

The foundation of this master's thesis is based on the doctoral thesis published by Hanetho [8], the master's theses by Halvorsen [9] and Raasok [10], and the project work performed during the fall of 2014 by the author [11]. Through the work of Hanetho, the potential for developing coatings on metal surfaces based on hybrid inorganic-organic sol-gel technology was showed. In the works of Halvorsen and Raasok, this technology in combination with hydrophobic coating materials was used to increase the water-repellency of surfaces. In the project work by the author, the coating material with the most promising results from the theses by Raasok and Halvorsen was chosen for further work, 1H,1H,2H,2H-perfluorooctyltriethoxysilane (from now on simply called β -silane). In this project the focus was on the steel substrate and to achieve a favourable topography to increase the water-repellency even more. The results showed that abrasive blasting with sand particles with a mean diameter of 150 μm gave promising results. A contact angle of 134.5° was achieved.

1.2 Aim of Work

The goal of this thesis is to further the understanding of the link between topography, hydrophobicity, and icing behaviour. As described is icing a costly problem, and effort should thus be put into the enhancement of the understanding of ice-phobic materials. This understanding may further lead to being able to develop surfaces that ease the deicing process, or even diminish icing completely. By mimicking the hierarchical structure of hydrophobic surfaces found in nature, through inducing micrometric- and nanometric roughness, and subsequent coating, super-hydrophobic behaviour will be developed and the icing behaviour of such surfaces examined. Both the crystallisation of supercooled water on the surface, along with the melting behaviour will be investigated.

In detail, the micrometric roughness will be developed by the same sand blasting procedure used in previous work. For the nanometric roughness, ZnO-nanowires will be synthesised using a hydrothermal method. The combination of the two will thus give a hierarchical structure which will subsequently be coated with the hydrophobic fluorosilane precursor from previous work. The effect of coating on the topography will be investigated by deposition using dip-coating and vapour deposition. Through this, further work with the superior method can be performed. The icing tests will be performed by mimicking sea spray icing, and the subsequent melting of the crystallised ice in room temperature.

The substrates, corrosion resistant AISI 316-steel, are chosen due to the frequent use in industry. To be able to develop anti-icing behaviour on such steels is of high interest. For use in industry, the mechanical properties of the induced roughness is of significant importance in order to reduce maintenance of treated surfaces. The mechanical properties will however not be addressed in this thesis.

Chapter 2

Theory

2.1 Wetting

As everywhere in the universe, nature strives to minimise its energy. It can either be by lowering the potential energy of a ball on top of a hill by rolling it down, or through a chemical reaction where the product has a lower internal energy than its reactants. This is also the case by wetting of a surface. When a droplet hits a surface, two new interfaces will form; the interface between the droplet and the gas phase, and that between the droplet and the surface. How the droplet behaves in contact with these two phases is dependent on which of the two phases it prefers. The preferred phase is the phase with which the droplet can come in contact and create a minimum of interfacial energy. Say that the energy of the gas-droplet interface is low compared to that of the surface-droplet interface, the droplet will strive to increase the gas-droplet interface area at the expense of the surface-droplet area. In this example, the droplet may wet the surface as shown in Figure 2.1(a). If however, the energy of the surface-droplet interface is lower than that of the gas-droplet interface, nature will strive to minimise the gas-droplet area, thus resulting in a behaviour shown in Figure 2.1(b).

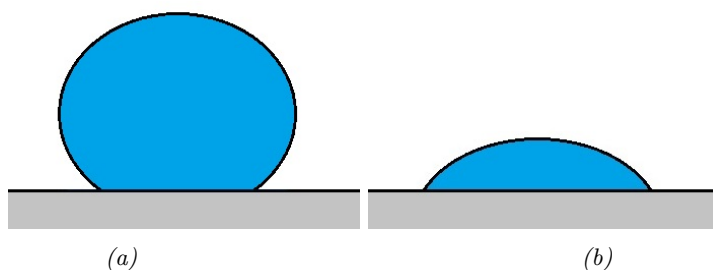


Figure 2.1: How a droplet wets a surface when the droplet-surface interfacial energy is (a) high and (b) low.

The wetting of a surface can be described through the droplet's contact angle, θ , shown in Figure 2.2. If the droplet wets with a low contact angle value, it is said that the wetting of the surface is good. The opposite, a high contact angle value, means that the wetting is poor. As already described, the wetting behaviour is a direct consequence of the minimisation of the energy in the system. This is mathematically described for a smooth, homogeneous surface by the Young-Laplace equation [12];

$$\gamma_{sv} = \gamma_{sl} + \gamma_{lv} \cos \theta \quad (2.1)$$

where γ_{sv} is the interfacial energy between the surface and the gas phase, γ_{sl} between the surface and the liquid, γ_{lv} between the gas phase and the liquid, and θ is the contact angle with which the liquid wets the surface. This is shown schemetically in Figure 2.2.

If the liquid in Figure 2.2 is water and the gas phase air, the contact angle in Equation 2.1 will be a measure of the hydrophobicity, or hydrophilicity, of the *surface*, being the only phase not already set. In this thesis we will focus on hydrophobicity, the ability of the surface to repel water. If the contact angle is greater than 90° , the surface is said to be hydrophobic [13]. However, there is a limit to which degree one can adjust the hydrophobicity of the surface solely by tailoring the interfacial energies. This limit is 120° for smooth and homogeneous surfaces [12]. To be able to develop superhydrophobic surfaces, defined as surfaces with a contact angle greater than 150° , other means are necessary [12, 14].

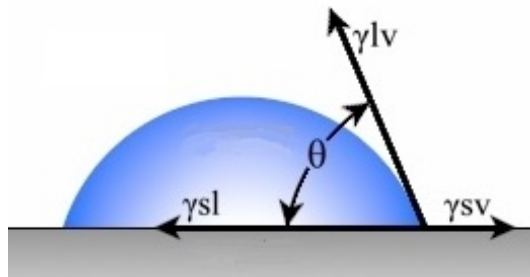


Figure 2.2: The figure shows a droplet wetting a surface and how the interfacial energies affect the wetting behaviour. The figure is adapted from the webpages of Ramé-Hart Instrument Co. [15].

2.1.1 Superhydrophobic Surfaces

The inspiration for the development of superhydrophobic surfaces comes from nature. In 1977 Barthlott and Neinhuis studied over 200 plants with superhydrophobic behaviour, where the Lotus leaf showed superior properties [16]. This led to the birth of the “Lotus concept” in 1992 [16]. What is so special with the Lotus leaves is the hierarchical structure of the surface, depicted in Figure 2.3. Nanometric roughness is present on top of a micrometric roughness, along with the presence

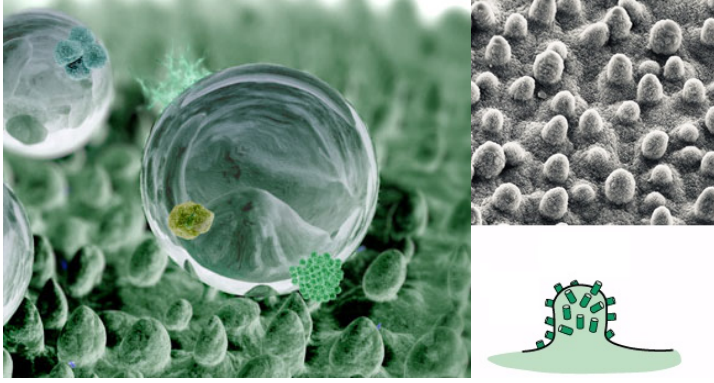


Figure 2.3: The surface of the lotus leaf consists of a hierarchical structure, with nm-scaled roughness on top of μm -scaled roughness. The figures are adapted from Dumé and the webpages of Nanostart AG [18, 19].

of a hydrophobic wax [13,17]. This combination leads to the possibility of reaching superhydrophobic contact angle values.

As pointed out earlier, the Young-Laplace equation only applies for smooth and homogeneous surfaces, meaning that a new model is needed to find a correlation between the contact angles of a surface, the interfacial energies, and the roughness. In 1936 Wenzel introduced a model for calculating the contact angle on a rough surface [20]. This model uses the Young-Laplace equation to calculate the contact angle, θ_e , and multiplies it with a roughness-factor, r , which is the ratio of the actual area the droplet wets the surface, over the projected area.

$$\cos \theta_r^w = r \cos \theta_e \quad (2.2)$$

In 1944 Cassie and Baxter introduced another equation for calculating the contact angle for a different type of wetting [21]. As in the Wenzel equation, the Cassie-Baxter equation uses the Young-Laplace contact angle, and adjusts it with a roughness factor, f , which is the fraction of the area where the liquid is in direct contact with the surface.

$$\cos \theta_r^{CB} = f \cos \theta_e - (1 - f) \quad (2.3)$$

The two equations, Wenzel and Cassie-Baxter, describe two different ways of wetting a surface. In the Wenzel state the droplet will penetrate the grooves. For the Cassie-Baxter case, the droplet will not penetrate, but rather stay suspended over the grooves, trapping air inside. A combined state is also possible. The three states of wetting are depicted in Figure 2.4. For hydrophobic purposes the Cassie-Baxter wetting is favourable, as the droplets are in contact with a smaller surface area and therefore easier to remove by influence from wind, gravity, or slight inclinations [13,22].

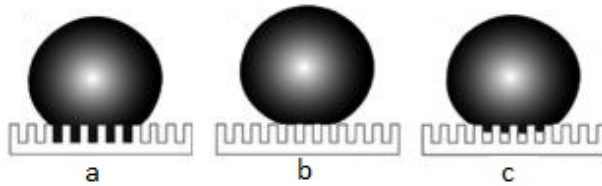


Figure 2.4: (a) Wenzel-, (b) Cassie-Baxter-, and (c) combined state of wetting. The figure is adapted from Xia and Jiang [23].

It is not enough to develop a surface roughness that will initiate a Cassie-Baxter wetting state upon deposition of a droplet, the roughness needs to be able to prevent transition of wetting state from Cassie-Baxter to Wenzel state upon influence from the surroundings. Kinetic energy from the impinging droplets and condensation of moisture from the surroundings may cause the state of wetting to "collapse" from the Cassie-Baxter to Wenzel state, with significant consequences regarding the hysteresis [24].

2.1.2 Contact Angle Hysteresis

Contact angle hysteresis is defined as the difference between maximum and minimum contact angle for a droplet on a surface, and occur due to chemical and topographical heterogeneity along with adhesion between the droplet and the surface [25, 26]. A requirement for superhydrophobicity is to keep the contact angle hysteresis of the wetting to a maximum of 10° [12]. The hysteresis can be explained by saying that a droplet of a given size has a range of contact angles with which it may wet the surface even though the surface remains unchanged throughout the different wetting tests [12]. There are several ways of measuring the hysteresis [25]. One of them is to deposit a droplet onto a surface and incline the surface, as shown in Figure 2.5. The surface is gradually tilted, resulting in changes of the contact angles, as shown in the figure. At the last moment before the droplet rolls off, the surface's advancing and receding angle can be registered. The difference between these two contact angles is the hysteresis [17]. Another method of measurement, used in this thesis, is explained in Section 2.1.5.

It is not always so that with high contact angles come low hysteresis values [27]. Although a surface may appear superhydrophobic by having a water contact angle greater than 150° , the water will not roll off of the surface when inclined, due to the adhesive forces being too strong. This is called the "Salvinia-" or "Petal effect", and can be regarded as the opposite of the "Lotus effect", where the droplets easily move around on the surface [28, 29]. The answer to why these two effects show important differences, even though they both show high contact angles lies both in the topography and chemistry of the surface. Both structures consist of hierarchical roughness as explained earlier. However, when investigating the surface of the Salvinia leaf, it has been discovered that the structure contains a hierarchical surfaces roughness with the presence of mostly hydrophobic wax, as the Lotus leaf,

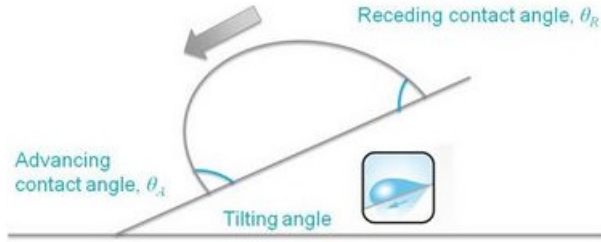


Figure 2.5: This figure shows a method for measuring contact angle hysteresis by inclination. The surface is tilted, during recording, until the droplet rolls off. The angles, both advancing and receding, are registered at the last moment before the droplet rolls off. Adapted from Biolin Scientific [25]

but approximately 2% of the surface is covered with hydrophilic cells [29]. This leads to a hydrophobic behaviour when wet, but the strong adhesive forces from the hydrophilic cells will cause large hysteresis values. Although this sounds like an undesired property at first, there are applications where such an effect could have huge potential, e.g. on the hull of ships to reduce friction [30]. Figure 2.6 shows how a retained air-layer on the surface would affect the friction on the surface.

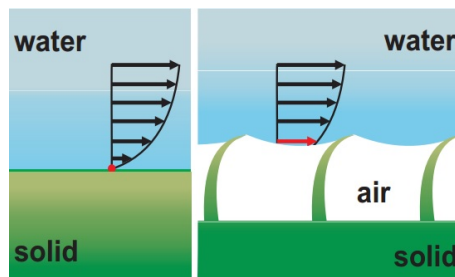


Figure 2.6: How a retained air-layer would affect the drag on a surface from moving water. Adapted from Barthlott et al. [31]

Achieving this effect is also possible without the presence of hydrophilic cells. When studying the petals of a red rose, also showing both high contact angle- and hysteresis values, important dimensional differences from the Lotus leaf was found. The dimensions of both the micro- and nano-structures of the rose petal are larger than of the Lotus leaves [32]. These changes may lead to another state of wetting than the desired Cassie-Baxter state. The larger dimensions may lead to the droplet being able to wet the grooves of the micro- and even the nano-structures, resulting in Cassie Impregnating state of wetting, or even full Wenzel. The Cassie Impregnating state of wetting is shown in Figure 2.7. In this state of wetting the droplet will wet the grooves between the micro-structures, but not the nano-structures,

resulting in both high contact angle- and hysteresis values [32]. If, in addition, the nano-dimensions are sufficiently large, full Wenzel-wetting may occur. This will result in lower receding contact angle- and higher hysteresis values than on an equivalent smooth surface, in contrast to Cassie-Baxter wetting where the opposite is observed [24].

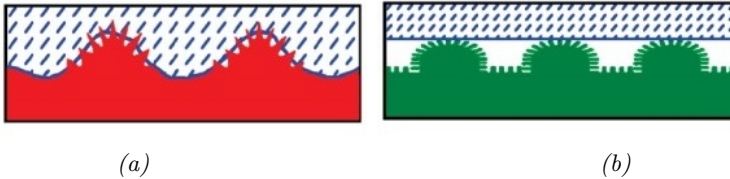


Figure 2.7: (a) Cassie Impregnating state of wetting compared to (b) Cassie-Baxter wetting. The figure is adapted from Feng [32]

Bhushan and Nosonovsky made in 2010 an overview over when four wetting states can be expected, with regard to peak-to-peak distance for the micro structure and the height of the nano structures, described by mass. It can here be seen that only a slight difference of the dimensions, or peak-to-peak distances, may have a significant effect on the wetting behaviour of the surface.

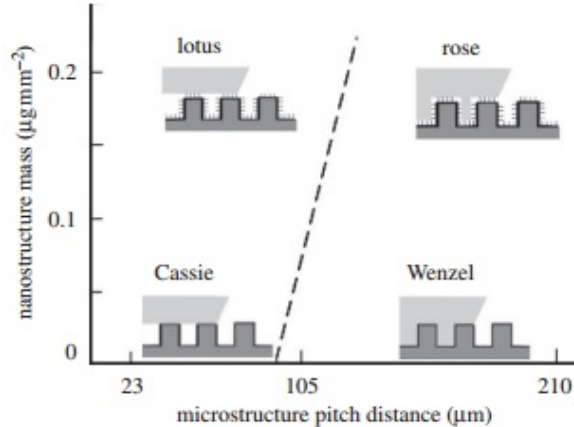


Figure 2.8: The graph shows what state of wetting that can be expected given the peak-to-peak distances of the micro-structure, and the height of the nano-structure on the surface. A nano-structure mass of zero means that only micrometric roughness is present. Here the limit between Cassie-Baxter and Wenzel wetting is a peak-to-peak distance of approximately $90 \mu\text{m}$. The rose state of wetting is synonymous with Cassie Impregnating wetting. Adapted from Bhushan and Nosonovsky [27]

2.1.3 Icephobicity

The term "icephobicity" was first introduced by Kulinich and Farzaneh in 2004 [33, 34], but in spite of growing interest worldwide the exact definition of icephobicity is still to be developed [34]. In 2013 Hejazi suggested a definition of an icephobic surface [35]. Even though this definition is new, it gives us an idea of what is needed from such a surface.

- Low ice-adhesion
- Delay of crystallisation
- Bounce-off effect

First is the ice adhesion. By measuring how much force is needed for the removal of ice from a surface, one can easily separate surfaces on which ice strongly adheres from more icephobic surfaces where the ice may slide off solely by the influence of wind or gravity. Hejazi suggests that the key parameters for icephobicity is the shear and normal force with which ice adheres to the surface, in the same manner as the contact angle and contact angle hysteresis are the key parameters for hydrophobicity.

The low ice adhesion can be looked upon as a property making the removal of ice easier but not reducing the crystallisation. The delay of crystallisation is however a promising property for icephobic surfaces. On a normal surface, supercooled water will instantaneously crystallise upon impact. However, on an icephobic surface the crystallisation will experience a delay, making the removal of water prior to crystallisation possible. The mechanism behind this delay goes back to basic heat-transfer combined with the state of wetting. In a Cassie-Baxter state of wetting a significant fraction of the contact area is replaced with grooves, containing nothing but air. Air is a poor conductor of heat. Thus, when a droplet comes in contact with a cold surface, the heat-transfer from the "hot" droplet to the colder surface will occur slower, and the droplet will experience a delay before reaching a temperature where it freezes. However, if the droplet has a temperature already below that of freezing, the reduced heat-transfer will have no effect. Here, nucleation needs to be depressed. As Cao et al. found, the energy barrier needed for crystallisation is dependent on the particles sizes on the surface [36]. The smaller they are, the more energy is needed to initiate crystallisation. For particles with diameters of less than 50 nm, the energy barrier is too large for icing to occur. This is shown as a graph in Figure 2.9.

Lastly, Hejazi mentions the bounce-off effect. An icephobic surface should have the ability to repel incoming water droplets. By bouncing supercooled water droplets, both the crystallisation delay and the hydrophobic nature of the surface come into play. Normally, a supercooled water droplet would instantaneously freeze upon impact with a surface. However, due to the crystallisation delay and no nucleation sites, the droplet will not freeze but rather stay liquid. The hydrophobic nature of the surface, having high interfacial energy with the newly-arrived droplet, will

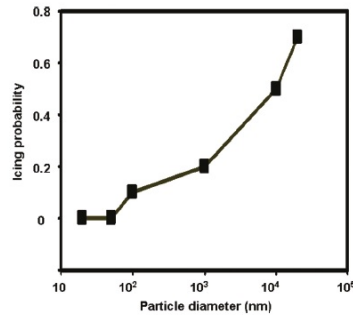


Figure 2.9: The probability of icing on a surface as a function of the size of the particles on the surface. The graph is adapted from Cao et al. [36]

strongly repel the droplet, causing it to bounce off of the surface. As mentioned, the bounce-off property is dependent on the surface being highly hydrophobic, which makes it hard not to discuss the link between icephobicity and hydrophobicity.

2.1.4 The Hydrophobicity-Icephobicity Relationship

For quite some time it was believed to be a direct correlation between hydrophobicity and icephobicity. Through many studies, arguing both for and against this belief [12, 13, 35–38], it has now become widely accepted that there is no *direct* correlation. This means that a hydrophobic surface will not necessarily also be icephobic, but an icephobic surface may be hydrophobic.

The delayed crystallisation was addressed for the icephobic surfaces, and is mainly due to the state of wetting. To achieve delayed crystallisation, one will have to develop a surface which is barely in contact with incoming droplets and as a result of such behaviour, the surface will show a high contact angle value. However, the mechanisms here are not quite the same. The delayed crystallisation is solely dependent on the minimisation of contact between the two components, and thus can the hydrophobicity of an icephobic surface be looked upon as a consequence, and not a prerequisite.

The bounce-off effect may be a product of the hydrophobicity of a surface. When a droplet falls down on an icephobic surface, the desire is for it to bounce off before nucleation. In order for this to happen, the surface must be superhydrophobic. With this in mind, it seems like also here the correlation between the two phobicities are strong. However, the nucleation of the droplet must also be taken into consideration, and it is here the correlation ends. As described earlier, Cao et al. found that the critical size of nucleation is approximately 50 nm. With structures with dimensions below this, icing will not occur. This critical size is of significant different magnitude than that for superhydrophobicity, where particles as big as 10 μm may be small enough [36].

Lastly, the ice-adhesion. It is obvious that when a droplet crystallises while in

the Cassie-Baxter wetting state the total adhesion between the ice-droplet and the surface will be lower than when crystallised on a flat surface, due to the significant decrease of contact area. If the correlation between the two phobicities was direct, as earlier belief, one would expect the adhesion strength of ice to decrease with increasing contact angles. This is not the case. Instead, Kulinich and Farzaneh suggested in 2009 that the hysteresis had a more important role regarding the ice adhesion strength [39]. By plotting measurements of shear stress on ice adhered on superhydrophobic surfaces, the authors found a linear correlation between the ice adhesion strength and the contact angle hysteresis, shown in Figure 2.10(a). However, Meuler et al. pointed out that by extrapolating the linearity shown in the figure, a surface with no hysteresis at all would still experience ice adhesion. Instead they found a direct correlation between the ice adhesion strength and the practical work of adhesion of a water droplet; the work needed to remove a droplet from a surface:

$$[1 + \cos\theta_R] \quad (2.4)$$

where θ_R is the receding contact angle [40]. With this, Meuler adjusted the linearity originally calculated by Kulinich and Farzaneh, so that when extrapolated, the ice adhesion strength would be zero when the receding contact angle reached 180° (theoretically maximum). The adjusted graph is shown in Figure 2.10(b).

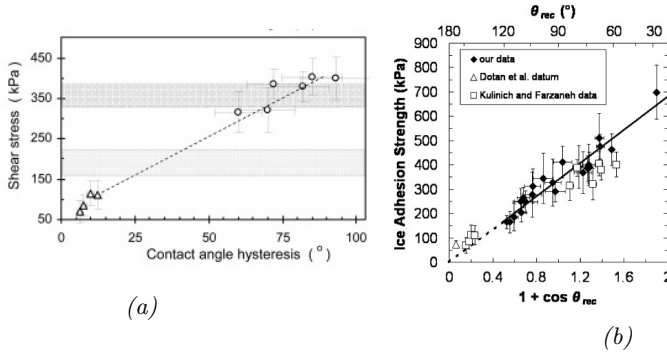


Figure 2.10: Ice adhesion strength as a function of (a) contact angle hysteresis and (b) receding contact angle. The graphs are adapted from Kulinich and Farzaneh [39], and Meuler et al. [40].

2.1.5 Characterisation of Wetting Behaviour

The wetting properties of a surface can be best measured using optical tensiometers. In addition to the contact angle, this kind of equipment can also measure interface- and surface tension, surface free energies, and even contact angle hysteresis, among other properties [41].

Contact Angle

When measuring the water contact angle of a surface, the pipette, number 2 in Figure 2.11, is programmed to deposit a droplet of desired volume onto the surface of the sample. The sample is placed on a movable table, number 1 in Figure 2.11. The camera, number 3, will record both the deposition of the droplet, and the behaviour of the droplet after deposition. The software will automatically recognise the interfaces between each of the phases and calculate the contact angle.



Figure 2.11: An optical tensiometer showing the (1) movable table on which the sample is placed, (2) the syringe from which a droplet is deposited, and (3) a recording camera. Adapted from the web pages of Biolin Scientific [41]

Hysteresis

The method of measuring the contact angle hysteresis used in this thesis is through extraction of water from, and injection into the droplet. A droplet is deposited onto the surface and the tip of the pipette is placed inside the droplet, as depicted in Figure 2.12. Through slow injection of more water, the droplet will grow in volume and the contact angle increase. The contact angle continues to increase until a certain value where the system rather increases the contact area between the droplet and the surface. At this moment the contact angle value is fixed and called the ascending contact angle. The receding contact angle is found by subsequently extracting water from the droplet. The contact angle will decrease to a point where the system rather decreases the contact area. At this point the receding angle can be found.

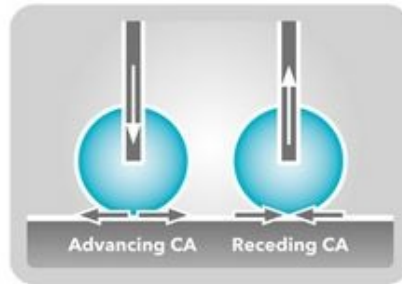


Figure 2.12: A method for measuring the contact angle hysteresis by extraction from and injection into the droplet. When water is injected the surface contact area will increase accordingly, and the ascending contact angle can be measured. The receding contact angle can be measured by the same manner, by extraction of water and reduction of surface contact area. Adapted from Biolin Scientific [25]

2.2 Stainless Steel

Steel is the most successful and cost-effective structural material available [42]. One of the reasons for its broad use is its ability to be tailored to a specific use, either through alloying, heat-treatment, or the possibility to cast complicated forms. Through the right alloying one can achieve a so called “stainless steel”. This steel is not completely stainless, and will in the wrong environments corrode like any other steel, e.g. in the presence of chloride-ions. However, in normal, and some cases even acidic environments, the steel will remain unstained and intact where other steels would lose mechanical and decorative properties.

In metallurgy, stainless steel is defined as steel containing 10.5 wt% or more chromium [43]. The reason for the ability to remain stainless is that the chromium will react with oxygen to form a thin Cr_2O_3 -film on the steel surface, as depicted in Figure 2.13. This film is extremely dense, hindering more oxygen to diffuse through the film and react with the iron to create rust. Through even more alloying, this film can become more stable in oxidizing environments and even resist acids and other chemicals.

In this project AISI 316-steel will be used, an austenitic stainless steel containing 17 wt% Cr, 12 wt% Ni, and 2 wt% Mo, along with 0.05 wt% C [44]. This steel has a high resistance against both corrosion and acids, and is often used in near-sea applications and offshore industry. In addition, the austenitic structure will not experience a sudden transition from ductile to brittle behaviour when the temperature drops [43], thus making this steel important as the search for oil heads north.

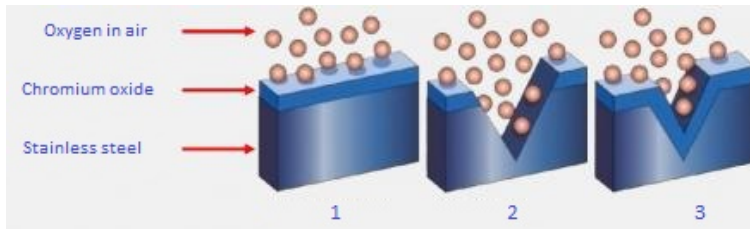


Figure 2.13: The figure shows how a steel surface is protected by a dense layer of chromium oxide, preventing oxygen from coming in contact with the bare steel (1). Even when the oxide layer is damaged (2), a new layer of chromium oxide will form when oxygen comes in contact with the surface, and prevent further corrosion (3). The figure is adapted from the websites of Cougartron [45].

2.3 Inducing Roughness

Roughness is needed to achieve a water contact angle greater than 120° . To increase the water contact angle even more a hierarchical roughness structure is beneficial. A hierarchical roughness structure is a combination of roughness on the micrometric and nanometric scale, much like the structure of the Lotus leaf, depicted in Figure 2.3.

The roughness can be measured by a range of different parameters, depending on what we want to highlight. The arithmetic roughness value, R_a , is the most common parameter in literature when investigating the roughness of a line, and is thus the most important parameter in order to compare results obtained. This value is calculated by:

$$R_a = \frac{1}{n} \sum_{i=1}^n |y_i| \quad (2.5)$$

where y_i is the height of peak number i , and n is the total number of peaks. Other values, such as maximum peak height and valley depth, peak count, and root mean squared roughness are also easily measured, but is less important regarding roughness for hydrophobic purposes.

In addition, equipment such as optical profilometers and AFMs offer the possibility to measure the roughness over an area, not just a single line. In this case, for the arithmetic value, the roughness is calculated by:

$$S_a = \frac{1}{MN} \sum_{k=0}^{M-1} \sum_{l=0}^{N-1} |z(x_k, y_l)| \quad (2.6)$$

Although this will be a more representative value for the roughness of a sample, the arithmetic roughness value, R_a , still is the most common in literature, most likely due to the simplicity of the measurement.

2.3.1 Micrometric Roughness

In research papers there are usually two methods that are repeatedly mentioned when inducing micrometric roughness on steel; etching and abrasive blasting [14, 21, 46, 47]. As already mentioned in Section 1.1, the author found in previous work that abrasive blasting showed the most promising result. Only abrasive blasting will thus be addressed in this thesis [11].

Abrasion Blasting

Abrasion blasting is performed by acceleration of small, hard particles onto a surface, as depicted by Figure 2.14. On impact these particles will remove impurities or paint, prepare the surface for subsequent coating, or even harden the surface, minimising the risk of fatigue [48]. In this thesis, the roughness caused by the procedure is what is desired. This method is a cost effective and scalable method



Figure 2.14: The principle of abrasive blasting. Small, hard particles are shot from a nozzle with great speed. The particles treat the surface through abrasion, leaving the surface smoother, rougher or cleaner, depending on the use.

for its use [14]. Abrasive blasting can be performed with a variety of particles, where sand is most common and will also be used in this thesis.

The result of sand blasting is principally dependent on the particle size. For hydrophobic applications, a high roughness with a small peak-to-peak distance is beneficial. Frank et al. found that the smaller the grains are when sand blasting, the better the surface morphology would be [14]. This was also confirmed by the work of the author, when comparing the roughness after abrasive blasting using sand particles ($\sim 150 \mu\text{m}$ diameter) and glass beads ($180\text{-}300 \mu\text{m}$ diameter) [11].

2.3.2 Nanometric Roughness

A hierarchical structure of roughness is beneficial in achieving even higher water contact angles. For the development of nanometric roughness there are typically two main approaches; top-down and bottom-up. Guo, He and Beckford [21, 49, 50] all suggest a bottom-up method, with slightly different methods. Where He and Guo both develop a nano-structure from ZnO, Beckford uses amorphous Si. All three methods involve the creation of seeds, and a subsequent growth of the nano-structure. The structures are shown in Figure 2.15.

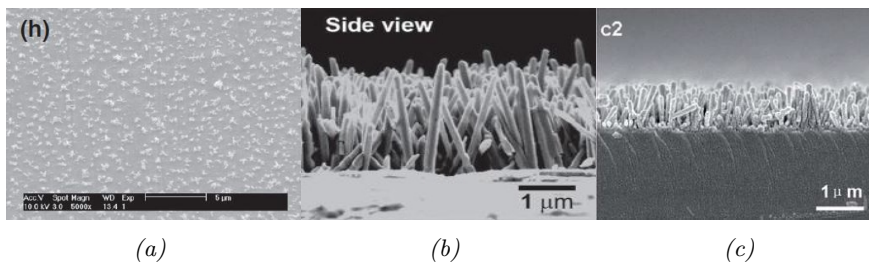


Figure 2.15: The pictures show nano-structured surfaces by a bottom-up method. (a) Amorphous Si structures on a stainless steel substrate. (b) ZnO-nanowires grown on a stainless steel substrate. (c) ZnO-nanowires grown on a glass substrate. The pictures are adapted from Beckford, Guo and He, respectively. [21, 49, 50]

Top-down is the approach which Vorobyev and Guo applied using a femtosecond laser [51]. Platinum, brass, and titanium samples were treated with laser to create intrinsic hierarchical roughness, depicted in Figure 2.16. The potential using this method is enormous. Not only are both the micrometric and nanometric roughness developed simultaneously, but the use of external hydrophobic coatings is futile, meaning the mechanical properties of the surface are solely determined by the material being treated [51]. The contact angle and hysteresis achieved with this method was reported to be 158° and 4° , respectively.

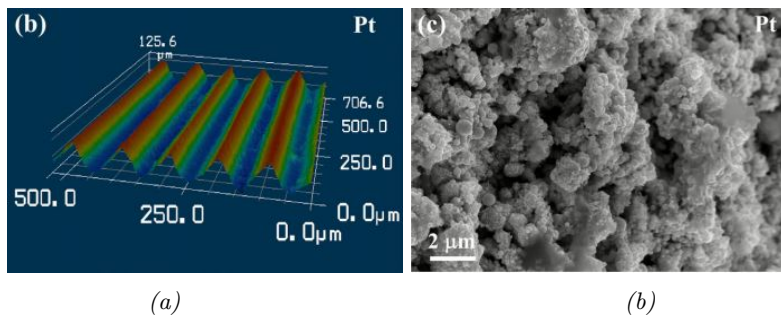


Figure 2.16: A hierarchical surface texture made on a platinum surface by femtosecond laser. (a) shows a modelled recreation of micrometric waves developed on the surface, whereas (b) shows a SEM-image of the nanometric roughness. The pictures are adapted from Vorobyev and Guo [51].

ZnO-nanowires

In this thesis we will focus on creating nanometric roughness by one-dimensional growth of ZnO-nanowires (ZnO-NW). The synthesis of these ZnO-NWs is widely used, mainly due to the promising properties regarding electronics, optics and photonics, and is therefore broadly applied for UV-laser-, photodetector-, gas-sensor-, and solar cell purposes [52, 53]. There are several methods to perform such a synthesis; the vapor phase synthesis, solution phase synthesis, hydrothermal method, and others [52]. In this thesis we will focus on the hydrothermal method.

The hydrothermal method is widely used [49, 52–61] due to the fact that this method can be applied on all kinds of substrates [52]. As it often is with widely used techniques, there are small varieties with which they are performed. First, a short introduction will be given to the more usual ways of performing this synthesis, before the role of each individual parameter is addressed.

What all techniques have in common is the two-step process; seeding and growth. The seeds are usually synthesised by solving zinc acetate in a solvent solution and deposited on the surface. The solvent is mainly ethanol [49, 53, 58], although alternatives can also be used [54, 57]. In addition to the solvent, surfactants and pH-adjusting agents may be added [54, 59]. The deposition of the seeds onto a surface may be done by spin coating [55, 57, 58], dip coating [58, 59], inkjet printing [54],

or even manually depositing single droplets on the substrate [53]. As a result of this seeding step, a thin layer of ZnO-seeds will be developed on the surface of the sample, as shown by an example from Wu et al. in Figure 2.17. In order to ensure adhesion of the seed-layer to the substrate, heat-treatment is needed. This heat-treatment may last from 20 minutes to 2 hours at a temperature of 95 to 350°C [49, 50, 53, 54].

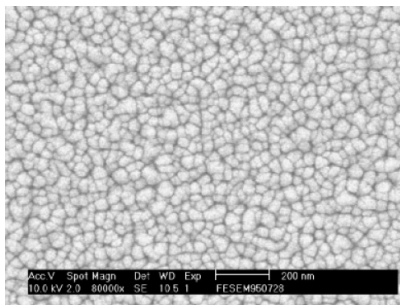
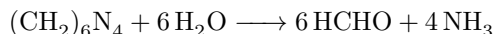


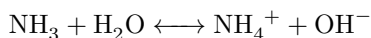
Figure 2.17: A seed-layer and its grains developed on a surface through deposition and heat-treatment of zinc acetate. The picture is adapted from Wu et al. [61]

The last step in the synthesis of ZnO-NWs is the growth. This is performed by a hydrothermal method in equimolar aqueous solution of normally hexamethylenetetramine (HMTA) and zinc nitrate [49, 54–56]. The precursors are mixed with deionized water, resulting in a concentration ranging from 1 to 100 mM, heated to 85–95°C, and held at this temperature for several hours. Other precursors than HMTA and zinc nitrate may be used, as will be addressed later, but HMTA is most often used due to its advantage in producing high-quality ZnO-NWs [52, 62]. The reactions when using HMTA is the following [63]:

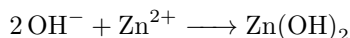
- Decomposition reaction:



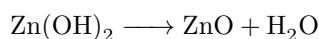
- Hydroxyl supply reaction:



- Supersaturation reaction:



- ZnO-wire growth:



The dimensions of the nanowires synthesised by this method is highly dependent on the parameters mentioned earlier. For example will the concentration of the equimolar aqueous solution used during growth directly affect the diameter of the nanowires [56], whereas the length is dependent on the duration of the hydrothermal growth process [53]. In the following sections the role of each parameter will be addressed more thoroughly.

Effect of the seeding layer The texture, thickness, and the grain size of the ZnO-seed layer will affect the quality of the nanowire growth [52]. As the thickness of the seed-layer increases, diameter increases and the density and length decreases [52, 64], as can be seen in Table 2.1. In addition, the heat-treatment affects the seed-layer. Heat-treatment is needed to ensure adhesion between the seed-layer and the surface, along with alignment, resulting in a perpendicular growth. For the adhesion and alignment of the seeds 150-200°C proves to be enough [53]. However, it has been suggested that heat-treatment should be performed with a temperature of 350°, resulting in best results regarding the subsequent ZnO-NW growth [60]. Heat-treatment at temperatures above 200°C will result in growth of the grains in the seed-layer. By an increase in the grain sizes, the NW diameter will experience an increase as well. This has no particular effect on the density [61].

Table 2.1: The diameter, density and length of ZnO nanorods corresponding to the thickness of the seed layer. Reproduced from Ghayour [64].

Thickness of the seed layer [nm]	Diameter of ZnO nanorods [nm]	Density of ZnO nanorods [μm^{-2}]	Length of ZnO nanorods [nm]
20	30	213	1052
40	36	209	1007
160	51	184	998
320	72	169	967

Effect of Precursor Concentration Other precursors than HMTA may be used. NaOH, Na₂CO₃, ammonia and ethylenediamine are also applicable chemicals. HMTA is however most often chosen due to the process being able to be carried out at temperatures below 100°C, in addition to the high-quality ZnO-NWs already mentioned [52]. The role of the zinc nitrate is mainly to provide Zn²⁺ ions, and may well be substituted with e.g. ZnCl₂ [62].

Notice that earlier it was mentioned that the growth solution consisted of an equimolar concentration of HMTA and zinc nitrate. Experiments performed by Wang et al. showed that by varying the zinc nitrate/HMTA-ratio, no significant effect was observed on the diameter or the density of the NWs. The aspect ratio, length/diameter, was however noticed to be at its largest at a zinc nitrate/HMTA-ratio of unity [65]. The zinc nitrate concentration proved to be of more interest. By increasing the zinc nitrate concentration from 8 mM to 40 mM, an increase in diameter from 43-70 nm was observed, along with an increase in length from

65 to 320 nm [65]. In addition, the zinc nitrate proved to have a significant role regarding the density of the NWs, as found by Xu et al. From concentrations of 0.1 mM to 5 mM, the density would increase from 55 to 108 wires/ μm^2 . By further increase, the density would remain approximately steady with a slight decreasing tendency [66].

Effect of Growth Temperature Experiments performed by Sugunan et al., where ZnO-NWs were grown with growth temperature of 65 °C and 95 °C. No significant change of dimensions were observed, and Sugunan suggests therefore that the influence of growth temperature on the growth is insignificant, compared to that of precursor concentration [67].

Effect of Growth Time The growth time will affect both the diameter and the length of the NWs, along with the aspect ratio. The results found by Yuan et al. and Baruah and Dutta [60,68] suggest that as long as the precursor concentration is high enough, both diameter and length will continue to grow. When the precursor concentration depletes, the diameter will stop growing even though the length continues. By replenishing the precursor, the diameter may start to grow again. If the diameter of the NWs is left to grow over a long period of time, they will eventually coalesce and form a ZnO-film [52].

Effect of Solution pH The nucleation and growth of ZnO is sensitive to the pH of the solution. If the solution is acidic, the final shape of the ZnO will be decided through competition between growth and etching of the NWs [69]. The total growth rate is thus greater in alkaline solutions where etching is absent. However, in solutions with an initial alkaline pH (8-12), the nanostructures developed will be in the form of flower petals, and not one-dimensional wires or rods. The two forms are shown in Figure 2.18. The conclusion drawn by Baruah and Dutta [69] is thus to initiate the growth procedure with a fairly acidic solution, pH 6.4, so that NWs, and not petals would nucleate. During the growth of 5 hours the pH would increase to about 7.3, where the fastest growth rate was observed.

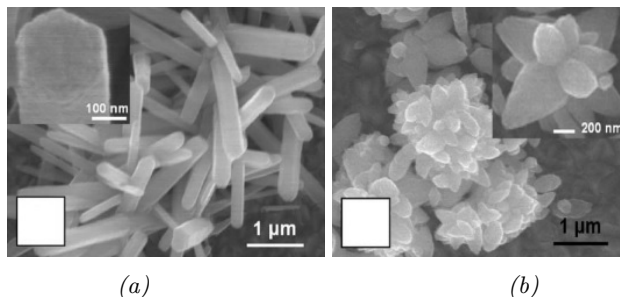


Figure 2.18: When the initial pH of the growth solution is acidic (a), the ZnO will grow as rods. When alkaline (b), the ZnO will grow in the form of flower petals. The pictures are adapted from Baruah and Dutta [69].

2.3.3 Surface Characterisation

Two different methods will be used in order to characterise the surface structure of the samples; a Scanning Electron Microscope (SEM) and a profilometer, see Table 2.2. The SEM is the most important equipment used, but the theory behind the microscope will not be addressed in detail.

Table 2.2: An overview of the equipment used for surface characterisation.

Equipment	Purpose
Scanning Electron Microscopy	Qualitative analysis of surface structure
Profilometer	Quantitative analysis of surface roughness

Profilometer

A profilometer is used to investigate the surface of a sample. This can be done either optically by measuring reflection, or mechanically with a stylus scraping the surface and detecting movement in vertical direction. The latter is carried out using a laser beam reflected off of the head of the cantilever, and detected by a photodiode. When the stylus meets topography whilst scanning the surface, it will shift vertically causing the reflection of the laser to shift accordingly. An illustration of the stylus profilometer is shown in Figure 2.19.

Many profilometers also offer measurements over an area. This can not only give information about the roughness, but can also be used to detect defects on the surface [70].

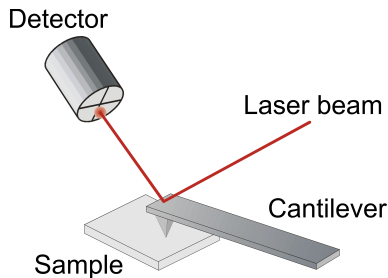


Figure 2.19: The principle of a stylus profilometer. A cantilever scans the surface of a sample and shifts vertically when encountering roughness. The laser beam reflected off of the cantilever will shift accordingly. The shift is recorded by the detector and analysed. The figure is adapted from the webpages of ETH Zürich [71]

2.4 Sol-Gel Synthesis

The solution-gelation (sol-gel) method is a cost-effective, simple and safe method of producing high-purity compounds. The fact that complex shapes and thin films can easily be produced with mild chemical conditions, low temperature, and with the use of easily purified reactants makes this method promising and widely used [72].

2.4.1 Overview

The basis of this method is the making of a solution. Dependent on further processing films, ceramics, particles, aerogels or fibers can be developed, as shown in Figure 2.20. The sol-gel method can be divided into six steps, where some of the reactions involved may occur simultaneously [72]:

1. Hydrolysis
2. Condensation
3. Gelation
4. Ageing
5. Drying
6. Densification

Only hydrolysis, condensation and gelation will be explained in detail, as the three later steps are negligibly present in this thesis.

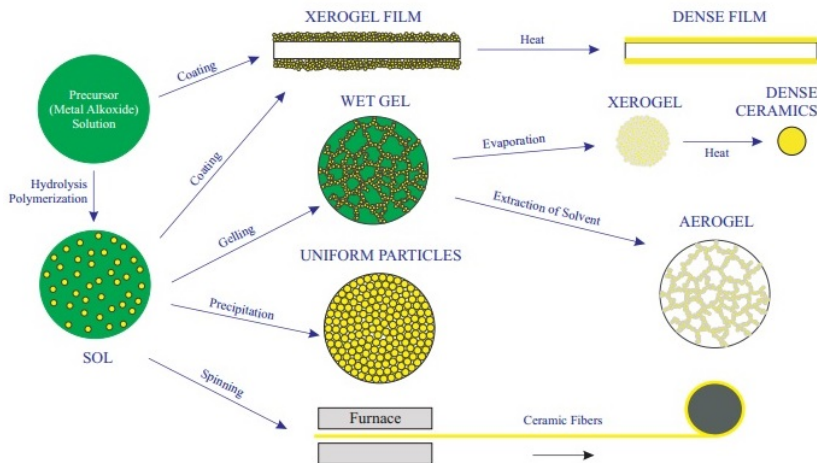


Figure 2.20: The sol-gel method can be designed to produce a long range of different products. The figure is adapted from Raasok [10].

2.4.2 Synthesis

Hydrolysis and Condensation

The hydrolysis and condensation reactions are the first to occur during the sol-gel process, and will occur more or less simultaneously. A precursor is first solved in water, as water has to be present for the hydrolysis to occur. Often, due to the hydrophobic nature of many precursors, alcohol is additionally needed to ensure dissolution. In Figure 2.21 a highly used precursor, tetraethoxy silane (TEOS), for the sol-gel process is depicted, along with a ternary phase-diagram of TEOS-water-alcohol. On the phase-diagram the correct proportion of water and alcohol in order to solve the precursor can be found. TEOS is not the precursor used in this thesis, but is adapted for explanation.

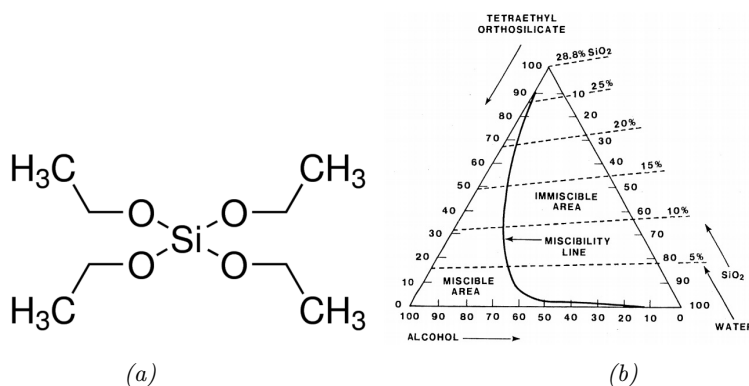


Figure 2.21: (a) The molecular structure of TEOS, a highly used precursor for the sol-gel method. This is not the precursor used in this paper, but is used for explanation purposes. (b) Ternary phase-diagram of TEOS, water and alcohol (for pure ethanol, the miscibility line is shifted slightly to the right [73]) The presence of SiO_2 are due to an equilibrium between the TEOS and SiO_2 . The figures are adapted from the webpages of Sigma-Aldrich, and Brinker and Scherer [73, 74]

Once the precursor is solved, the hydrolysis and condensation will begin. For a neutral sol the hydrolysis reaction will proceed slowly. In Figure 2.22 the rates for both hydrolysis and condensation are visible. Even though the condensation speed is high, hydrolysis is a prerequisite for the condensation to occur, and the total reaction will therefore move slowly.

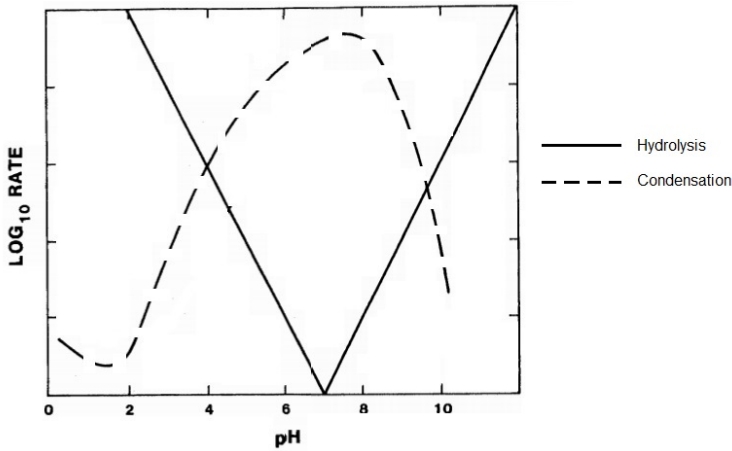


Figure 2.22: The relative speed of the reactions depends on the pH of the solution. Note that the hydrolysis is at its slowest at neutral pH-values, whereas the condensation is at its highest. For an overall fast reaction, a compromise has to be made. The graph is adapted and modified from Brinker and Scherer [73]

In order to speed up the process, a catalyst is normally added. The catalyst, an acid or a base, will shift the pH to an acidic or alkaline value and the process will speed up. Not only does the pH affect the rate, but also the reaction itself. Figure 2.23 shows the chemical reactions occurring during hydrolysis and condensation. For an acid-catalysed sol, the hydrolysis reaction will be predominant, whereas the condensation reaction dominates for base-catalysed sols [8, 75].

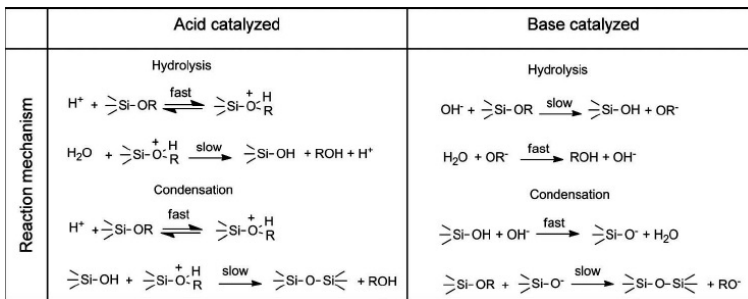


Figure 2.23: The hydrolysis and condensation reactions depending on acid- or base catalysis. The figure is adapted and modified from Chang and Ring [75]

Gelation

During condensation of polymers and aggregation of particles, clusters will form and eventually come in contact with each other. The end result will be one continuous cluster, stretching from one end of its container to the other. This giant cluster is called a gel. The process from single particles, via bigger clusters, and ending as a gel is shown in Figure 2.24. At this gelation point, picture 5 in Figure 2.24, the system will suddenly experience a rise in viscosity [73]. The time of gelation is highly dependent on the preparation steps, e.g. the water/precursor-ratio; more water means a greater distance between each cluster, and thus will the total gelation time increase significantly [72, 73].

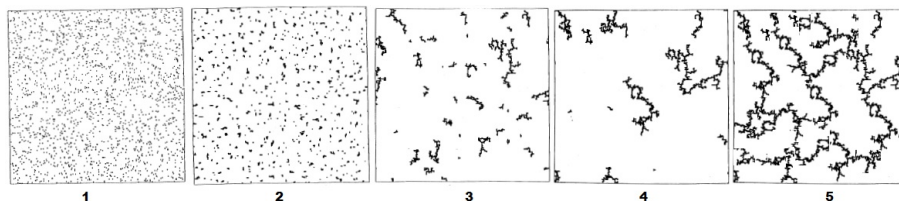


Figure 2.24: These pictures show how small particles will tend to interact to form larger clusters, and subsequently form separate branches. These branches will with time interact with each other, and form a continuous system throughout the container, forming a gel. These pictures are adapted and modified from Brinker and Scherer [73]

To develop a coating using the sol-gel method, as is the case in this thesis, the coating procedure needs to be carried out before gelation occurs, as can be seen from Figure 2.20. The gelation process will increase the viscosity of the sol, even before full gelation occurs. A rise of viscosity may have undesired results regarding the thickness of the coating when dip-coating is performed. In order to achieve an as thin as possible coating layer, a fresh sol is needed.

What catalyst is used does also have a significant influence on the coating. Through acid catalysis, linearly chained molecules will be created, whereas clusters will form through base-catalysis. The growth and gelation process for both acid- and base-catalysed sols when used as a coating can be seen in Figure 2.25. The long chains developed through acid-catalysis will align upon deposition onto a surface to create a dense, thin film, whereas the clusters from base-catalysis will result in a thicker, less dense film. The combination of the two sols will result in cross-linked random aggregates that further result in a highly porous coating [8].

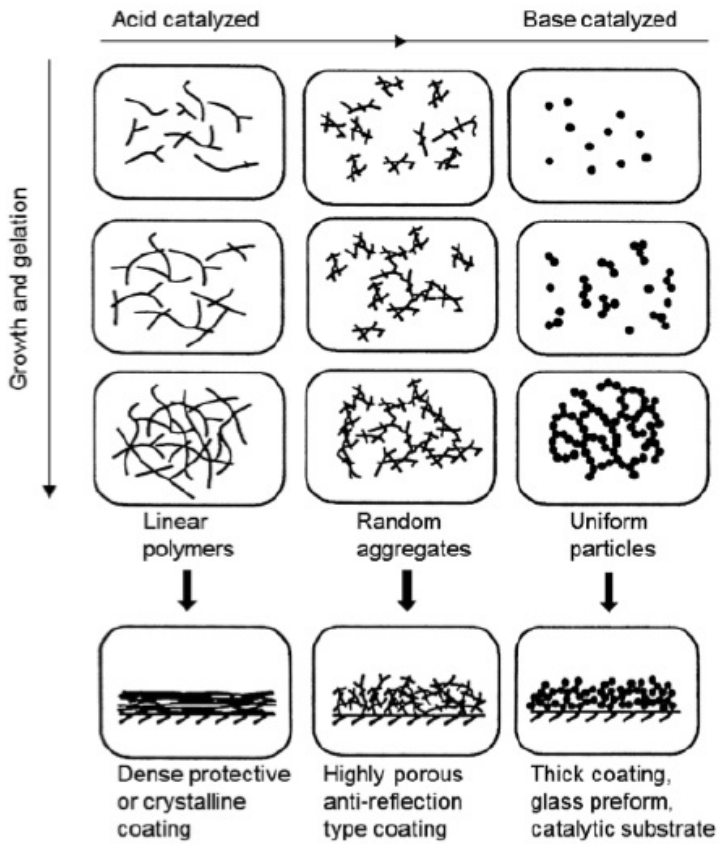


Figure 2.25: Growth and gelation process, and the resulting coating layer of an acid- or base catalysed sol. The figure is adapted from Hanetho [8]

2.5 Deposition

The covering of a surface with i.a. alkoxy-silanes is called "silanization" [76]. Surfaces possible to silanize are surfaces containing hydroxyl-groups, which in turn will react with the silanes and create bonds. Metal oxides, e.g. Cr_2O_3 on stainless steel, are such surfaces [77]. Due to the need of hydroxyl-groups on the surface, plasma-cleaning with O_2 prior to deposition may be beneficiary, as it will promote hydroxylation of the surface [77]. For the deposition of hydrophobic coatings after plasma-cleaning, it is important to acquire a thorough coating as the plasma-cleaning alone will render the surface hydrophilic [77].

There are several ways to perform such a silanization. Dip-, spray-, spin-, and drawdown coating are relatively inexpensive methods due to the independence of costly equipment [78]. In this paper two methods will be used. Dip-coating as a batch process which is an easy method to develop a uniform coating layer on the substrate. For this reason dip coating is the most widely used technique for deposition of films [79]. The other method is a simplified method of vapour deposition. The theory behind both of these methods and the chemistry behind the bonding will be addressed here.

Before the methods are described in detail, the author wishes to stress that for the use of dip-coating a sol has to be synthesised, as described in Section 2.4. Vapour deposition does *not* need a sol, and can be applied using simply the precursor.

2.5.1 Dip-Coating

The whole process of dip-coating can be divided into five stages; immersion, start-up, deposition, drainage, and evaporation. Although the process is divided, the underlying chemical and physical processes are mostly overlapping [78,79].

The thickness of the film deposited is related to several factors, where the gravity, viscous drag, and surface tension are the deciding forces [78,79]. If the pull-up speed of the substrate and the viscosity of the liquid are high enough, the surface tension may be neglected. The resulting formula is given by a balance between the gravity $F_g = \rho gh$ and the drag force $F_d = \mu U/h$, where U is the velocity of the substrate relative to the liquid surface, h the thickness of the coating, ρ the density of the liquid, μ the viscosity, and g the gravitational constant:

$$h = c_1 \sqrt{\frac{\mu U}{\rho g}} \quad (2.7)$$

For newtonian liquids, like the solutions processed in this paper, the proportionality constant, c_1 , is approximately 0.8 [78]. Notice from the equation that the thickness of the deposited solution will increase with increasing withdrawal speed, a phenomenon that seems contradictive at first glance. By lower values for the viscosity and pull-up speed, the surface tension can no longer be neglected, and the resulting formula becomes [78]:

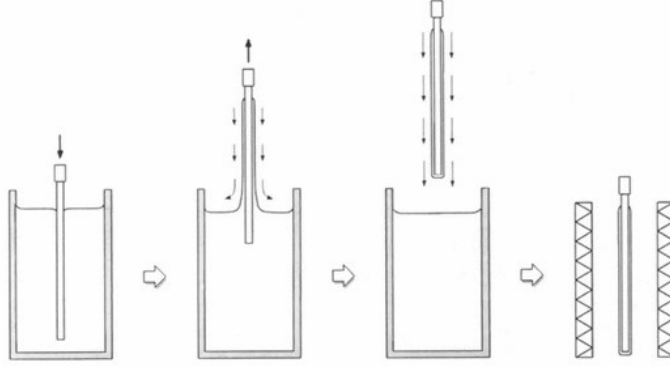


Figure 2.26: From left to right: 1) The substrate is immersed in the solution with a given speed. The solution starts to wet the substrate. 2) As the substrate is withdrawn, the abundant solution will flow off. 3) Some drainage may continue, although evaporation of solution is the main process. 4) The deposited solution may be heat-treated in order to optimise the properties of the resulting coating. The figure is adapted from Puetz [79]

$$h = 0.944 \left(\frac{\mu U}{\sigma} \right)^{\frac{1}{6}} \left(\frac{\mu U}{\rho g} \right)^{\frac{1}{2}} \quad (2.8)$$

Due to a "start-up end"-effect the deposited film will be thin at the edges on top of the substrate, and thickens to the value given above over some distance. This can be described as a function of x ;

$$h = \sqrt{\frac{\mu x}{\rho g t}} \quad (2.9)$$

where x is given as the length from the top of the substrate to the surface of the liquid, t is the time since the top edge of the substrate left the surface, and the surface tensions are neglected.

During evaporation, which occurs above the surface level, the viscosity of the liquid on the substrate will increase before the liquid finally solidifies and creates a film. Even liquids that normally would not wet the surface of the substrate can through fast evaporation be utilized to develop films. A final heat-treatment step is often necessary to obtain the desired quality of the resulting coating [79].

To use this method as a deposition process, a machine is needed to control the speed with which the substrate is pulled out of the liquid, as this cannot be executed with desired precision by a human hand.

Bonding

When coating a surface with a sol, the creation of bonds will occur as depicted in Figure 2.27. The hydroxylated surface and the sol come into contact, and interact

through hydrogen bonding between the OH-groups. Through the finalising heat-treatment, covalent bonds and H_2O will be created.

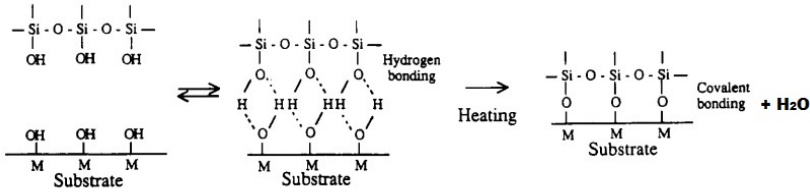


Figure 2.27: The bonding reaction between alkoxy silanes and hydroxyl groups on surfaces. The OH-groups from the silane and the surface come in contact through van-der-Waals bonds, and develop covalent bonds through heat-treatment. H_2O is additionally created in the reaction. The figure is adapted from Chovelon [80].

Viscosity

As explained above, the viscosity is of major importance in the dip-coating process, and will have a great influence on the thickness of the deposited coating layer. Viscosity is that property of a fluid which gives rise to forces that resist the relative movement of adjacent layers in the fluid [81]. This can be visualised using two parallel plates in relative movement, as Figure 2.28 shows. The fluid in contact with the faster moving plate will move along the plate with equal velocity. The adjacent fluid will move with slightly lower velocity, and the layer in contact with the non-moving plate will not move. This creates a linearity that describes a newtonian fluid.

$$\frac{F}{A} = -\mu \frac{\Delta v}{\Delta y} \quad (2.10)$$

This linearity is only the case for fluids that act as they are stacked in layers, i.e. laminar flow.

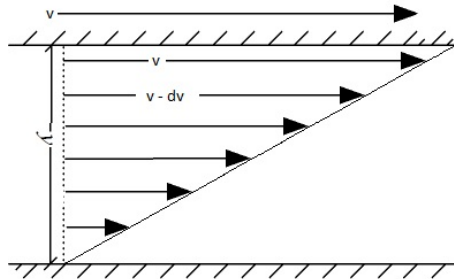


Figure 2.28: The figure shows the velocity profile of a newtonian fluid. The fluid will act as stacked in layers between a body moving with a velocity v , and a non-moving body.

2.5.2 Vapour Deposition

Here, some theory behind Chemical Vapour Deposition (CVD) will be given. The method used in this thesis is a simplified form of CVD. The simplifications will be addressed afterwards.

The definition of CVD, given by Choy, is "the dissociation and/or chemical reactions of gaseous reactants in an activated environment, followed by the formation of a stable solid product" [82]. This can be simplified to "condensation of gaseous reactants onto a substrate". The method is highly versatile, and through several improvements throughout the years, the method can be used to create thin films and coatings of semiconductors, ceramic fibres, metallic films, and even superconductors and ferroelectrics. Depending on what material the coating is made of, an external heating source may be needed, in order to achieve gaseous reactants.

The process consists of several steps, all visible in Figure 2.29 [82]:

1. Generation of active, gaseous reactants.
2. Transport of reactants into reaction chamber.
3. Gas-phase reactions forming intermediate species.
4. Absorption of the gaseous reactant onto the substrate.
5. Diffusion of the reactants to the crystallisation centre and subsequent growth.
6. Removal of by-products from the substrate.
7. Unreacted reactants or by-products removed from the chamber.

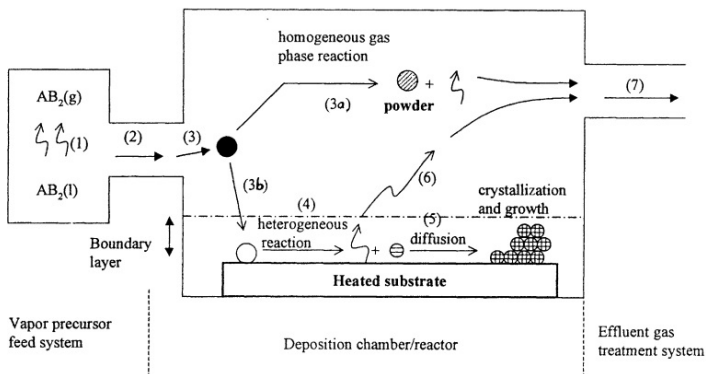
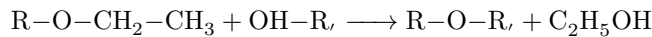


Figure 2.29: The steps involved in a Chemical Vapour Deposition procedure. Gaseous reactants are brought into the reaction chamber and condensate onto the substrate. Un-condensated reactants are subsequently removed from the chamber. The figure is adapted from Choy [82].

Vapour Deposition, as we choose to call the method used in this thesis, is far simpler. Here, the coating material is a highly volatile silane, meaning that no additional heating source is needed in order to create the gaseous reactants. The substrates and a container of the precursor is placed in a chamber in which vacuum subsequently is introduced. The silane will evaporate and saturate the atmosphere in the chamber. Once saturated, the silane will start condensing on the substrates, creating a film of gas-particles bonded through weak van-der-Waals forces.

Bonding

Due to the absence of sol in this depositing method, the bonding is likely to occur a bit differently than when dip-coating. On Figure 2.30(a) the molecular structure of the β -silane, which is used in this thesis, is shown. Through the vapour deposition the silane will come in contact with the surface and adhere weakly through van-der-Waals forces. Through a finalising heat-treatment step, covalent bonds will be created. In contrast to the structure of the sol, no OH-groups are present on the silane. Instead of bonding through the condensation of water, ethanol will be created:



In what degree such a silane will bond with the surface is unclear. As depicted in Figure 2.30(b), the silane has a tetrahedral structure with the fluorine-group stretching out on one end, the three ethyl groups on the others. If all ethyl-groups react as described above, the fluorine-group, being the hydrophobic group, will stretch out from the surface, as shown in Figure 2.30. However, if only one or two of these ethyl-groups react with the surface, the silane-molecule may bond lying down with one or two ethyl-groups accessible on the surface.

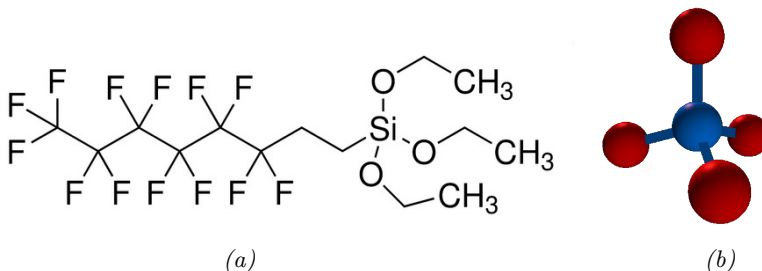


Figure 2.30: (a) The structure of the β -silane and (b) its orientation in a 3-dimensional space. The blue sphere represents the Si-atom, and the four red spheres represent the four branches bonded to the Si-atom.

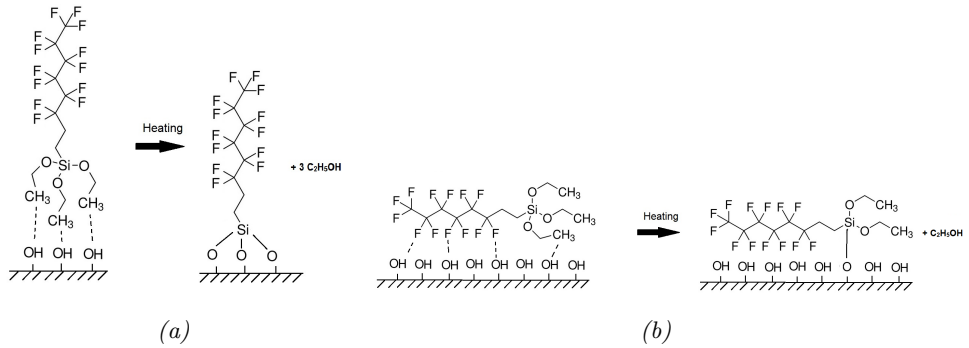


Figure 2.31: The bonding reaction between the β -silane and OH-groups on the surface. (a) shows the orientation of the precursor when all possible ethyl-groups develop bonds with the surface, while (b) shows a possible orientation when only one ethyl-groups develop a bond. The solid lines represent covalent bonds, and the dashed lines represent van-der-Waals bonds.

Chapter 3

Experimental

A rough overview of the experimental work performed is depicted as a flow chart in Figure 3.1.

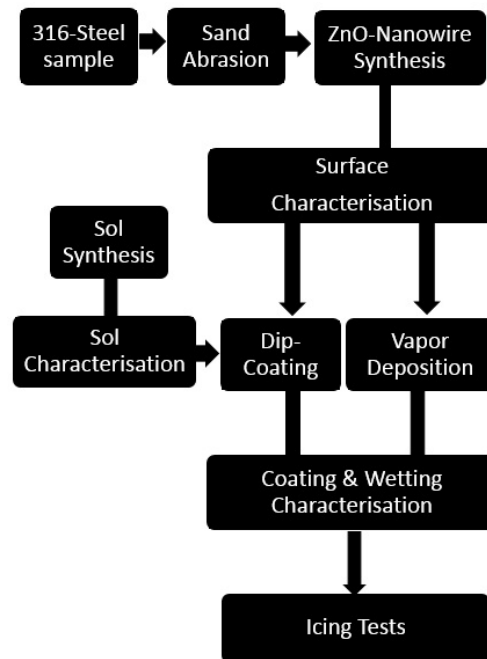


Figure 3.1: A flow chart presenting the experimental work performed in this thesis.

The samples used were of AISI 316-steel with the dimensions 15x10x2 mm. The thickness of 2 mm was chosen to maintain the shape of the samples after sand blasting which would introduce stresses in the surface and bend the samples if too thin. Furthermore, small samples were chosen to minimise the cost of the coating material needed and to simplify the process.

3.1 Inducing Roughness

3.1.1 Micrometric Roughness

Abrasion blasting with sand particles with a mean diameter of 150 μm was used to induce micrometric roughness on the samples. SINTEF's sand blasting cabinet, shown in Figure 3.2, was used during this procedure. The samples were held approximately 5 cm from the nozzle and prepared for 5 seconds each.



Figure 3.2: SINTEF's sand blasting cabinet in which micrometric roughness was induced.

3.1.2 Nanometric Roughness

Table 3.1 shows the chemicals used to synthesise the ZnO-NWs.

Standardisation

Before synthesis, a standardisation of the chemicals was performed. Given that both Zinc Acetate Hexahydrate (ZAH) and Zinc Nitrate Dihydrate (ZND) contain crystal water, it was necessary to establish the exact amount. Even though the formula contains information about this, variations for each batch may occur and must therefore be controlled. When the exact amount of crystal water is calculated, the amount of the chemical needed to achieve the desired concentration of the active ingredients can be found.

Table 3.1: The chemicals used during the synthesis of ZnO-NWs. The information is extracted from [83–87]

Chemical	Formula	Supplier	CAS
Zinc nitrate hexahydrate	$\text{Zn}(\text{NO}_3)_2 \cdot 6\text{H}_2\text{O}$	Sigma-Aldrich	10196-18-6
Zinc acetate dihydrate	$\text{Zn}(\text{CH}_3\text{COO})_2 \cdot 2\text{H}_2\text{O}$	Sigma-Aldrich	5970-45-6
Hexamethylenetetramine	$\text{C}_6\text{H}_{12}\text{N}_4$	Sigma-Aldrich	100-97-0
Ethanol	$\text{CH}_3\text{CH}_2\text{OH}$	VWR	64-17-5
Deionized water (18.2 M Ω ·cm @ 25°C)	H_2O	NTNU	7732-18-5

For ZND this was executed by solving 101.44 grams of the compound with 400 grams of deionized water. Approximately 0.7 grams of the solution was then transferred to a crucible and covered with a piece of Kaowool. Both the crucible and the Kaowool had been heat-treated at 1100°C for six hours to make sure any contaminations in the Kaowool would decompose. The crucible, now containing the solved ZND was heated from room temperature to 100°C with a rate of 50°C/h and held three hours, before further increase to 700°C with a rate of 200°C/h, and held six hours. The temperature was further decreased to 200°C and held at this temperature until retrieval to make sure no water would be absorbed. The crucible was transferred to a desiccator to minimise contact with water in the atmosphere. The exact weight of the crucible containing the ZND was measured before and after heat-treatment. Given that only the water would evaporate, leaving the zinc nitrate in the crucible, the correct amount of crystal water could be calculated.

For ZAH the same procedure was executed without dissolving the compound prior to heat-treatment. No standardisation for HMTA was needed.

Synthesis

The parameters chosen to synthesise ZnO-nanowires of desired dimensions, were found by trial-and-error and adjustments of parameters found in literature:

- Seeding: Manual deposition of droplets.
- Heat-treatment: 200 °C for 20 minutes.
- Soltution concentrations: 0.010 M.
- Growth temperature and time: 90 °C for 5 hours.

Seeding Steel samples, both sand blasted and not, were thoroughly cleaned by ultrasonic bath in acetone, ethanol, 10 % aqueous HCl-solution, and deionized water, respectively, for 5 minutes each, before being plasma-cleaned with oxygen for 10 minutes. Subsequently, a seeding layer was deposited on the surfaces by manually applying 3-5 droplets of 0.010 M zinc acetate in ethanol. After 10 seconds the substrates were rinsed with ethanol with a wash-bottle and blown dry with

argon-gas. This was repeated 5 times before heat-treatment at 140 °C for 5 minutes to ensure adhesion of the developed zinc acetate layer on the surfaces. To ensure complete coverage, the whole process was repeated. The samples were further put in the oven at 140 °C, and heated to 200 °C with a rate of 50 °C/h, and held for 20 minutes before cooling down to room temperature with a rate of 50 °C/h. The oven used with the placement of the samples inside is shown in Figure 3.3(a) and (b).



Figure 3.3: The oven, Carbolite 2 muffle furnace, and placements of the substrates inside the oven during heat-treatment. The samples were placed on an alumina-disc.

Growth For the growth process the samples were put one at a time in the sample holder, shown in Figure 3.4(a), which were to be placed inside an autoclave, depicted in Figure 3.4(b). The samples were to be placed horizontally face-down to ensure homogeneous growth, as explained by Rørvik [88]. The distance from the bottom of the autoclave to the sample was 18 mm.

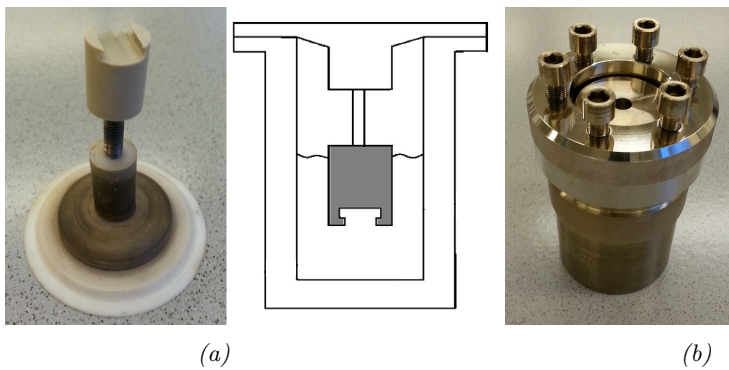


Figure 3.4: (a) The sample holder and its placement inside the (b) autoclave.

Before the sample holder was placed in its position, an equimolar 0.010 M aqueous solution of ZND and HMTA was quickly mixed at room temperature, with a total volume of 70 mL, and transferred into the autoclave. The pH of the solution was measured to be approximately 6, using the pH-meter Mettler Delta 340 from Mettler Toledo. The sample holder with the sample was subsequently immersed in the solution, and the autoclave thoroughly sealed to prevent evaporation. The sealed autoclave was put in the same oven as used during the heat-treatment of the seed-layer. The placement of the autoclave in the oven is shown in Figure 3.5. The autoclave was kept at 90°C for five hours before being retrieved without cooling. The sample was quickly removed from the sample holder, rinsed thoroughly with deionized water, and dried in the same oven for five minutes at 90°C.



Figure 3.5: The placement of the autoclave inside the oven during growth of ZnO-NWs.

3.1.3 Surface Characterisation

For the investigation of the developed ZnO-NWs a SEM was used. The parameters used during imaging is visible on the lower part of the SEM-images. A profilometer was additionally used in order to quantify the roughness induced through sand blasting, since the height and density of the peaks are difficult to quantify only by imaging.

Profilometer

The profilometer used was the Veeco Dektak 150, shown in Figure 3.6. The scan parameters are given in Table 3.2. The surfaces were blown dry with N₂-gas prior to measurements in order to remove dust and loosely adhered particles.

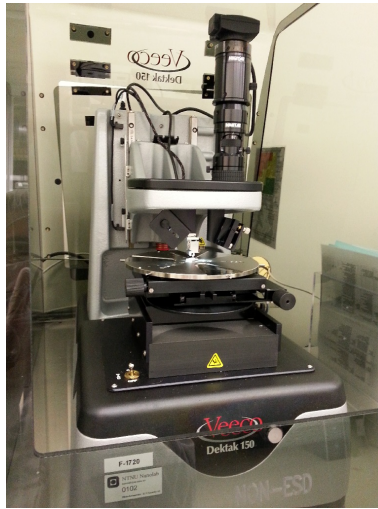


Figure 3.6: The Veeco Dektak 150 profilometer.

Table 3.2: The parameters used during roughness measurements of sand blasted samples.

Parameter	Value
Stylus radius	12.5 μm
Scan length	1000 μm
Duration	60 sec
Resolution	0.056 $\mu\text{m}/\text{sample}$
Force	3 mg

3.2 Synthesis of Solution

3.2.1 Chemicals and Sol Parameters

The precursor chosen for the sol was the β -silane. The molecular structure of the precursor is depicted in Figure 3.7. This precursor was chosen based on the work performed by Halvorsen and Raasok [9, 10].

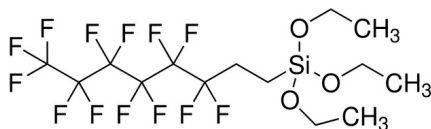


Figure 3.7: The molecular structure of the β -silane. The figure is adapted from the webpages of Sigma-Aldrich [89].

The sol recipe was also chosen based on the work performed by Halvorsen and Raasok, in addition to the results from previous work by the author [11]. The recipe is given in Table 3.3. The information needed to calculate the volumetric amount of each reactant is given in Appendix A. Information about the chemicals used during the synthesis is given in Table 3.4.

Table 3.3: The recipe of the solution by stoichiometric water/precursor- and solvent/precursor ratios. The recipe is adapted from Halvorsen and Raasok [9, 10]

Sol ID	Precursor	$n_{H_2O}/n_{Prec.}$	$n_{Solv.}/n_{Prec.}$	Solvent	pH
β -3R-40S-E-10	β -silane	3	40	Ethanol	10

Table 3.4: Chemical used during sol-synthesis. Information about the chemicals is extracted from [83, 87, 89, 90].

Chemical	Formula	Supplier	CAS	Function
β -silane	$C_{14}H_{19}F_{13}O_3Si$	Sigma-Aldrich	51851-37-7	Precursor
Deionized water (18.2 M Ω ·cm @ 25 °C)	H_2O	NTNU	7732-18-5	Solvent
Ethanol	CH_3CH_2OH	Sigma-Aldrich	64-17-5	Solvent
Ammonium hydroxide	NH_4OH	Sigma-Aldrich	1336-21-6	Catalyst

3.2.2 Synthesis Procedure

The precursor was dissolved in deionized water and ethanol in a 50 mL round-bottom flask. Before mixing, the water was adjusted to an alkaline solution (pH=10) using NH_4OH . The pH value was controlled with the pH-meter Mettler Delta 340 from Mettler Toledo. The solution was heated to 60°C with a heating mantle designed for 50 mL round-bottom flasks and held at this temperature for 1 hour. It was subsequently cooled to room temperature, and stored in a glass container at 5°C until further use. A magnetic stirrer at 350 rpm, along with a water cooled cylinder to prevent evaporation was used during the whole process. The setup is shown in Figure 3.8. The synthesis procedure was adapted from Halvorsen and Raasok [9,10].



Figure 3.8: The experimental setup of the sol-gel synthesis. A 50mL round-bottom flask was put in a heating mantle, and placed on a hot plate with a magnetic stirring function. A water cooled cylinder was placed on the round-bottom flask in order to condensate evaporated solution.

3.2.3 Sol Characterisation

The viscosity of the sol was measured using Haake RheoWin Mars III rotational rheometer from Thermo Scientific, shown in Figure 3.9. The measurement was performed immediately after synthesis, and carried out using constant shear rate (CR). Approximately 2 mL of the solution was measured at a temperature of 20 °C. The parameters used during measurements are given in Table 3.5.

Table 3.5: Parameters used during viscosity measurements of the sol.

Program	Shear rate [s^{-1}]	Time [s]	Number of measurements
Rot Ramp (step)	0.0010-500.0	180	100
Rot Time	500.0	30	100
Rot Ramp (step)	500.0-0.0010	180	100

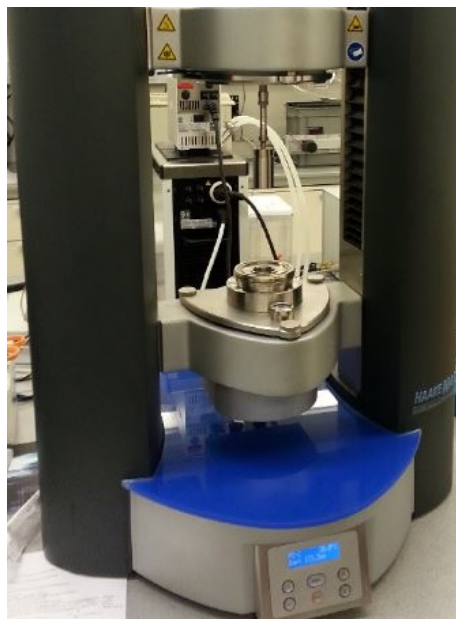


Figure 3.9: Haake RheoWin Mars III rotational rheometer from Thermo Scientific.

3.3 Deposition

Dip Coating

For the deposition of the solution onto the substrate a KSV dip coater was used, shown in Figure 3.10(a). The solution was transferred into a teflon-"well", shown in Figure 3.10(b), into which the substrate was dipped with the parameters shown in Table 3.6.

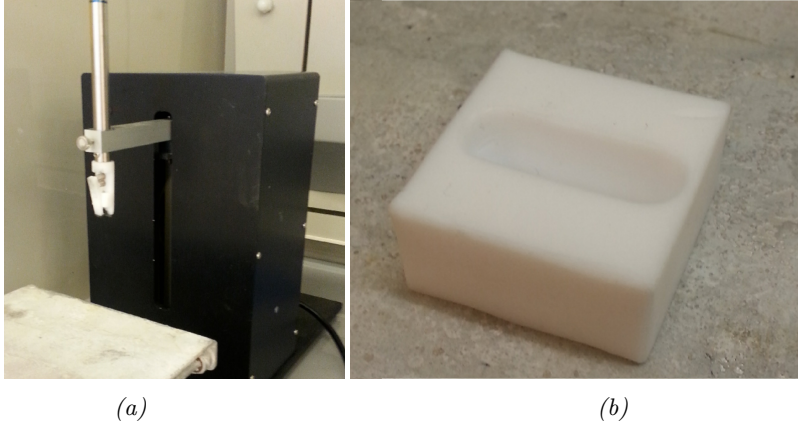


Figure 3.10: (a) The KSV dip-coater, and (b) the teflon-well in which the coating material was poured.

Table 3.6: The parameters used during dip-coating.

Parameter	Value
Immersion speed	170 mm/min
Holding time	10 min
Withdrawal speed	5 mm/min

After deposition the samples were heat-treated in order to evaporate remaining liquid and densify the coating. The samples were heated from 50 to 150 °C with a rate of 50 °C/h. The temperature was then kept at this temperature for 5 hours, before cooled down to 50 °C at the rate of 50 °C/h. Finally, all samples were rinsed with ethanol using a wash-bottle.

Vapor Deposition

The experimental setup of the vapour deposition is shown in Figure 3.11. Here, the samples and a container of the β -silane¹ were put inside a desiccator and placed under vacuum. To ensure that when vacuum was introduced only silane-particles

¹Remember: No sol-synthesis was needed for the vapour depositing method.

would be present in the atmosphere, the vacuum-pump was active for 5 minutes, before sealing the desiccator. After 10 minutes, the vacuum-pump was active for another 5 minutes. This was repeated three times, before the desiccator was sealed for the appropriate silanization-time. By this method, any remaining water, or such, would evaporate and be pumped out during the second or third vacuum-pumping. The samples were left in the desiccator for 22 hours after the third pumping-cycle. The period of 22 hours was found to be appropriate for this use through trial-and-error.

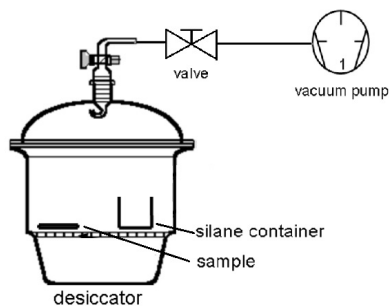


Figure 3.11: Experimental setup used during vapour deposition. Adapted and modified from Gilles [91]

After the samples were removed from the desiccator they were placed on a heating-plate, shown in Figure 3.12, and heat-treated at 100°C for one hour. This heat-treatment would ensure bonding between the precursor-molecules and the OH-groups on the surface of the samples. The samples were finally rinsed with ethanol using a wash-bottle.



Figure 3.12: The heating-plate on which the samples were treated after vapour deposition.

3.4 Wetting Characteristics

3.4.1 Water Contact Angle

The contact angle measurements were carried out using the Attension optical tensiometer from Biolin Scientific, shown in Figure 3.13. The software was programmed to deposit 8 μL of distilled water onto the surface. Upon deposition the software would automatically recognize the water-surface interface, and the contact angle was measured. Before measurements the tensiometer was calibrated using a given calibration ball.

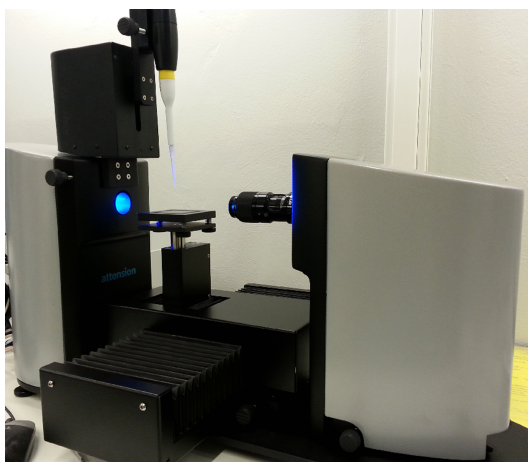


Figure 3.13: The Attension Theta T330 optical tensiometer from Biolin Scientific.

3.4.2 Hysteresis

The same equipment was used for the contact angle hysteresis measurements. A droplet with the volume of 8 μL was first deposited onto the substrate. The tip of the pipette was subsequently placed on the droplet, as shown in Figure 3.14. By this placement, the contact angle on the left side of the droplet would be undisturbed, thus being the focus for the measurements. Further, water was injected from the pipette and into the droplet with a rate of 1 μL per second for approximately 10 seconds. After the injection, the water was subsequently extracted from the droplet, with a rate of 1 μL per second.

The tensiometer shown in Figure 3.13 does not have a program designed for the measurement of hysteresis, thus manual control of the placement of the pipette along with the injection of extraction of water was needed.

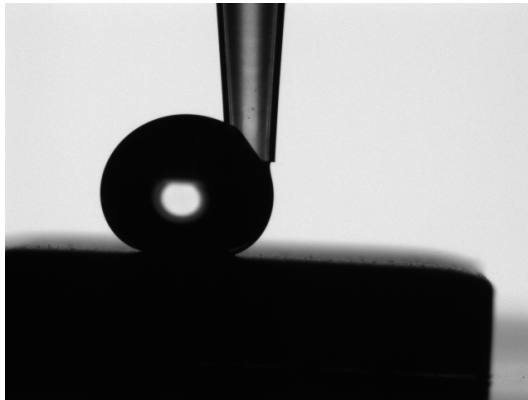


Figure 3.14: The pipette was placed on the right side of the droplet during hysteresis measurements, leaving the left side undisturbed.

3.5 Icing Characteristics

To investigate both the icing and deicing behaviour of the prepared samples, three experiments were carried out; investigating of the behaviour when exposed to single supercooled droplets, simulation of phenomena like sea spray icing, and melting behaviour when adhered ice is exposed to room temperatures.

During both experiments the samples were mounted on a 45°-tilted aluminium plate using a one millimetre thick, double-sided foam tape, placed on top of the plate as shown in both Figure 3.15 and 3.16. The thickness of the tape and the placement would minimise the risk of water droplets sliding down the plate and onto the samples during measurements.

The experiments took place in a walk-in freezer keeping a temperature of approximately -20°C. The equipment was placed inside the freezer 1.5 hours prior to the execution of the experiments in order to obtain the right temperature of the water. Deionized water (18.2 MΩ ·cm) was used during the experiments. After 1.5 hours the water was measured to hold a temperature of -0.2°C. The samples were placed in the freezer 15 minutes before execution, also to obtain subzero temperatures.

Single Droplet

A pipette was held 5 cm above each of the samples, and set to deposit 8 μL on the tilted samples, as shown in Figure 3.15. Pictures of each of the samples were taken after the droplets were deposited.



Figure 3.15: The experimental setup of the icing behaviour of a single droplet. The pipette was set to deposit 8 μL and held 5 cm above the samples. The samples were placed on a 45 °-tilted aluminium plate.

Spraying

The spray bottle containing supercooled water, visible in Figure 3.16, was held approximately 3 cm from the samples, and sprayed two times onto each of the samples. To better mimic sea spray icing, the spray bottle was adjusted to maximum dispersion. The icing behaviour was closely observed over a period of 5 minutes.

Deicing test

After the 5 minutes in the freezer, the plate with the samples was moved to room temperature where the deicing behaviour was observed.

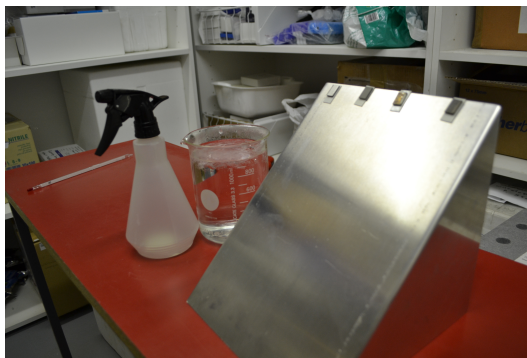


Figure 3.16: The sea spray icing experimental setup. Samples were mounted on a 45° tilted aluminum plate, and subsequently sprayed with supercooled water.

Chapter 4

Results

4.1 Surface Roughness Characterisation

In addition to the micro- and nano-structured steel samples, untreated steel samples were investigated. An image of such a surface can be seen in Figure 4.1. These steel samples are as delivered, thus not polished and therefore not entirely smooth due to the grain boundaries present as relatively superficial valleys. These surfaces will however be called smooth, as compared to sand blasted surfaces.

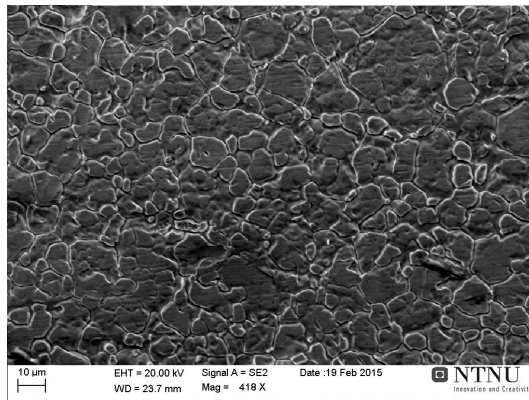


Figure 4.1: The SEM-image shows the surface of an as-delivered steel sample. The sample is tilted to better observe the topography from the grain boundaries.

4.1.1 Surface Morphology of Sand Blasted Samples

For the introduction of micrometric roughness, samples were blasted with sand particles with a mean diameter of $150\ \mu\text{m}$. Figure 4.2(a) shows a SEM-image taken of the surface of a sand blasted sample. Roughness measurements performed using a profilometer, example shown in Figure 4.2(b), resulted in a R_a -value and peak-to-peak distance given in Table 4.1.

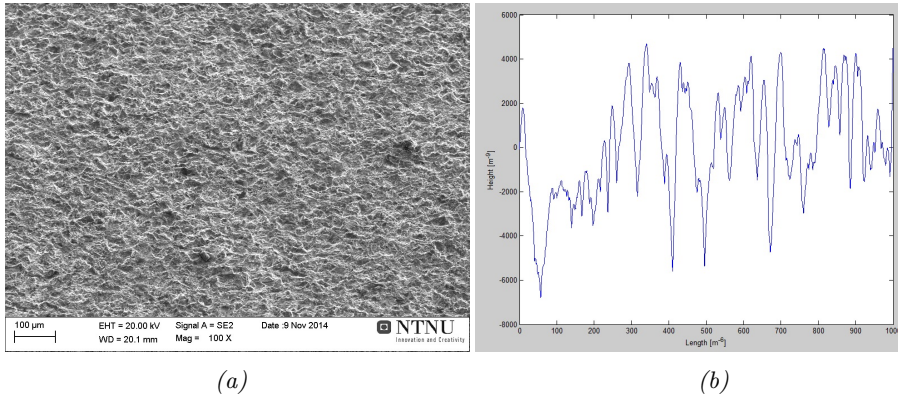


Figure 4.2: (a) SEM-image and (b) topography of a typical sand blasted sample. The topography is measured by a stylus profilometer.

Table 4.1: R_a -value and peak-to-peak distance of the sand blasted samples.

R_a -value [nm]	Peak-to-peak distance [μm]
1600 ± 148	59 ± 6.00^1

¹The peak-to-peak values was measured manually by counting the number of peaks with a minimum height of $4\ \mu\text{m}$ per measurement ($1000\ \mu\text{m}$).

4.1.2 Surface Morphology of Samples with ZnO-Nanowires

Figure 4.3 shows ZnO-NWs developed on a smooth steel surface. The approximate mean dimensions of the structures are; length: 500-700 nm, diameter: 50-90 nm, and density: $23\text{-}24 \mu\text{m}^{-2}$.

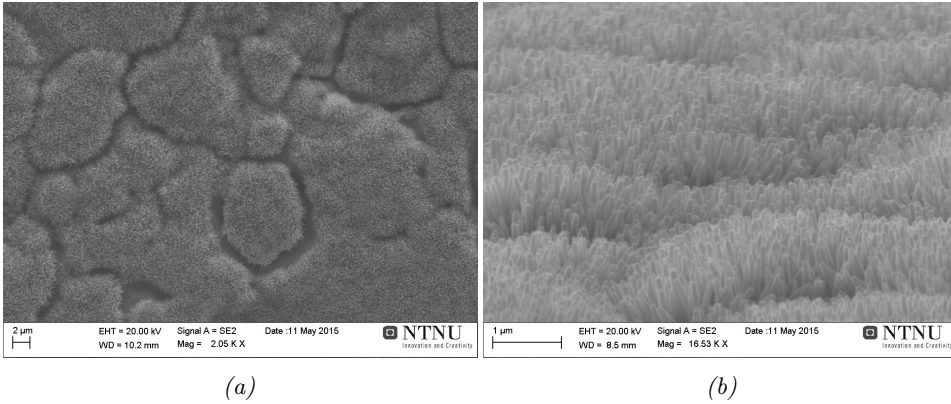


Figure 4.3: SEM-images of ZnO-nanowires on steel surfaces. (a) An overview over the homogeneous growth of the nanowires. (b) A magnified, tilted picture in order to see a more detailed structure.

4.1.3 Surface Morphology of Samples with Hierarchical Structure

Figure 4.4 shows ZnO-nanowires developed on a sand blasted steel surface. The approximate mean dimensions of the structures are; length: 250-500 nm, diameter: 150-200 nm, and density: $20\text{-}21 \mu\text{m}^{-2}$

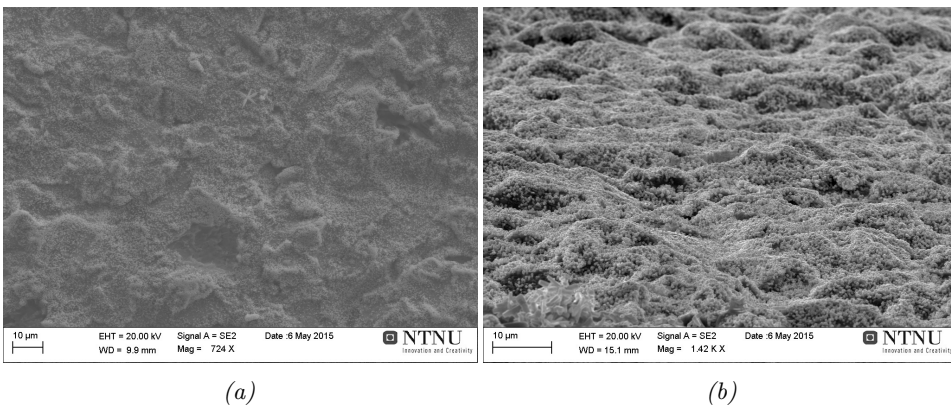


Figure 4.4: SEM-images of ZnO-nanowires on sand blasted steel surfaces. (a) An overview over the homogeneous growth of the nanowires. (b) A magnified, tilted picture in order to see a the hierarchical structure in more detailed.

4.2 Sol Characterisation

The viscosity measurement was performed immediately after synthesis, simultaneously as samples were coated. The value is given in Table 4.2, and is comparable to that of water at 5°C (1.519 mPa·s).

Table 4.2: The viscosity of the sol. The viscosity is comparable to that of water at approximately 5 °C [92].

Sol ID	η [mPa·s]
β -10-3R-40S-E	1.58

The sol was also studied in a SEM, see Figure 4.5, in order to investigate the presence of small particles in the alkaline sol, as explained in the theory section using Figure 2.25.

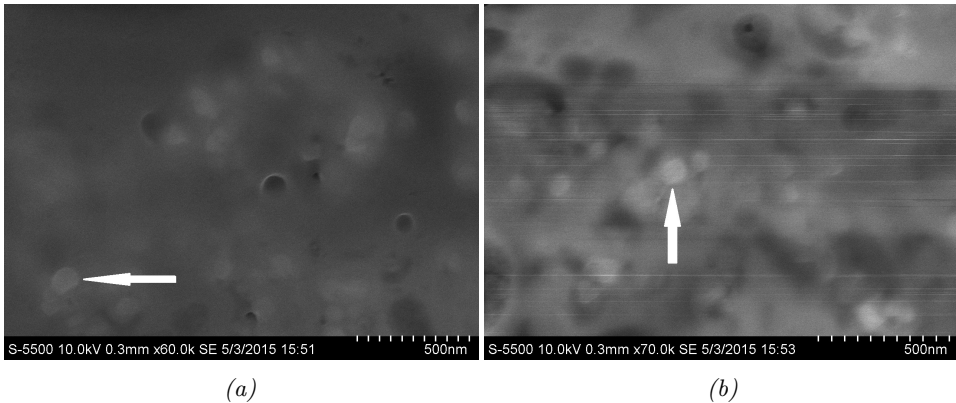


Figure 4.5: SEM-images of sol coated on steel substrates. Both (a) and (b) show the presence of small, spherical particles in the sol immediately after synthesis.

4.3 Coating and Wetting Characterisation

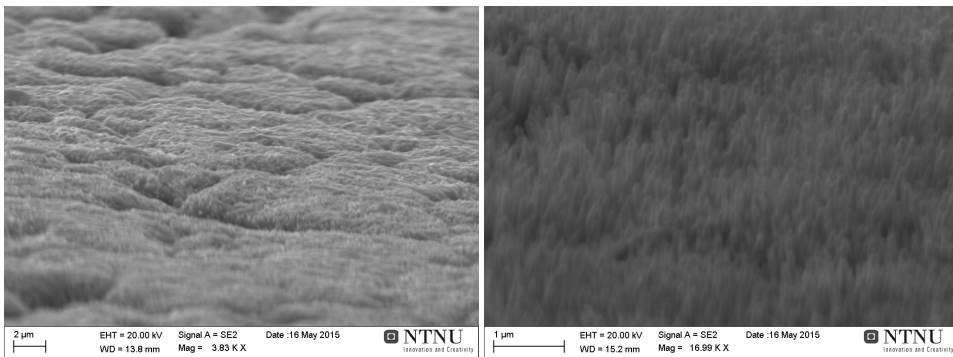
For the sake of simplicity abbreviations will be used from this point when addressing the different samples and how they are prepared. Table 4.3 gives an overview over the abbreviations used.

Table 4.3: An overview over the abbreviations used for the different samples.

Abbreviation	Preparation
DC-	Dip-Coated
VD-	Vapour-Deposited
U	As-delivered
S	Sand blasted
N	ZnO-NW
SN	Sand blasted & ZnO-NW

4.3.1 Surface Morphology after Coating

In order to see the effect of the two different coating procedures on the surface nano-structure, the N-samples were investigated with a SEM. One sample was coated using dip-coating, the other vapour deposited. The surfaces of the two can be seen in Figure 4.6. Notice that on Figure 4.6(a), the original rod-shaped structure of each individual ZnO-NW is hard to recognize due to the overlaying coating. On Figure 4.6(b) each ZnO-NW is clearly visible. Please note that the pictures are taken after coating with the β -silane, which is sensitive to the incoming electrons from the SEM, and distorts the pictures in some degree.



(a)

(b)

Figure 4.6: The effect on the nano-structure when using (a) dip-coating and (b) vapour deposition when applying the coating. Notice that on (b) the rod-shaped nanowires are clearly visible, whereas no such rods seem to be visible in (a), where the surface has become smoother.

4.3.2 Wetting Characterisation

Before the results from the wetting measurements are presented, the effect of ethanol-rinsing on the contact angles will be addressed. Figure 4.7 shows the contact angle measured on the same location on the same sample before and after ethanol rinsing. Clearly a significant increase of contact angle value after rinsing occurred. The example is taken from measurements performed on a VD-N-sample. The other samples did also experience an increase of contact angle, although not as significant. Note thus; all measurements given from this point are performed after rinsing with ethanol.

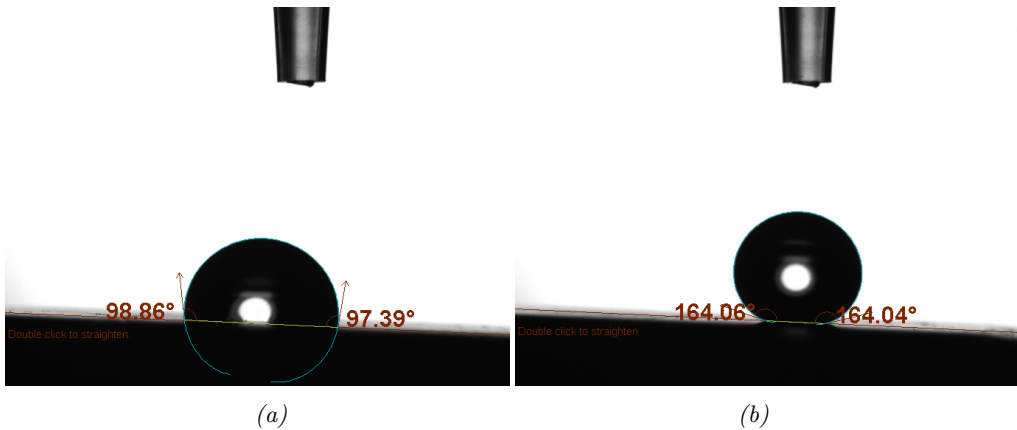


Figure 4.7: The effect of ethanol rinsing on contact angle values. (a) is before rinsing, and (b) after. An increase of contact angle value from approximately 98° to 164° was observed. All samples experienced an increase, the example here given is the most dramatic observed.

Contact Angle Measurements

Average contact angles on all substrates, with and without micro- and nano-structure, along with before and after coating, are shown in Table 4.4.

Table 4.4: Average contact angle, including standard deviation. The measurements are performed 10 seconds after droplet deposition.

Sample	U	S	N	SN
Un-coated	72 ± 8.79	90 ± 17.97	90 ± 20.00	64 ± 9.40
DC-	131 ± 1.05	154 ± 1.57	154 ± 1.00	158 ± 4.13
VD-	125 ± 1.31	153 ± 1.05	161 ± 3.96	164 ± 1.54

Contact Angle Hysteresis Measurements

The hysteresis measurements were only performed on the vapour deposited samples, due to the higher contact angle values. Hysteresis measurements were also performed on the U-sample for comparison. During all measurements it was noticed that the droplet seemed to adhere strongly to the surface immediately when come in contact with even a small area of the surface. Figure 4.8 shows in what degree a droplet would be deformed before contact between the needle and droplet was lost. The contact area when the droplet initially came in contact with the surface and when fully deformed was unchanged.

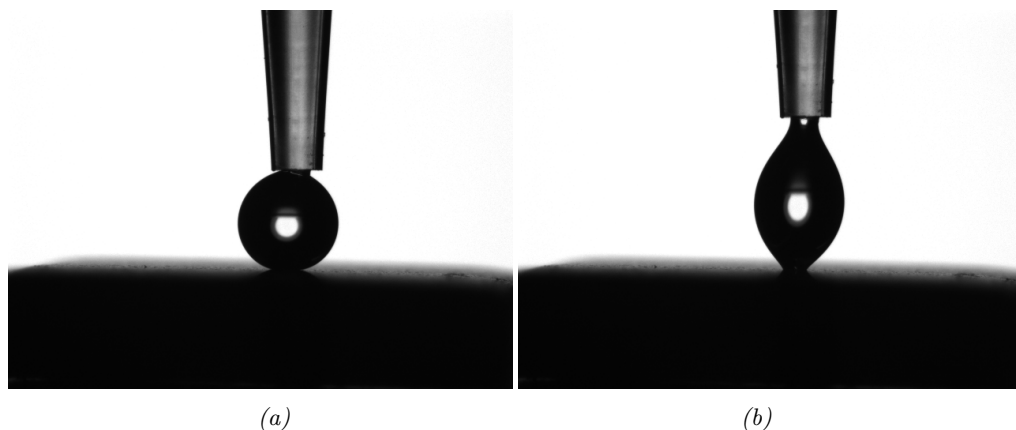


Figure 4.8: An example of high adhesion between droplet and surface. (a) The droplet when come in contact with the surface. (b) The droplet right before the needle lost contact with the droplet.

The measured ascending- and receding contact angles, along with the resulting hysteresis values, are given in Table 4.5. An example of how the measurements were performed is given in Figure 4.9. As explained in Section 3.4.2, a droplet was deposited onto a surface, and subsequently injected with more water from the pipette. Upon the injection, the contact angle value would rise until a maximum value, where rather the contact area between the droplet and the surface expanded, instead of the contact angle. The contact angle measured at this point was the ascending contact angle, visible for the VD-S-sample in Figure 4.9(a). The receding angle was found by subsequently extracting water from the droplet. The contact angle would decrease, until a point where rather the contact area between the droplet and the surface decreased, leaving the contact angle approximately steady, visible for the VD-S-sample in Figure 4.9(b). The same procedure was followed for all samples given in Table 4.5.

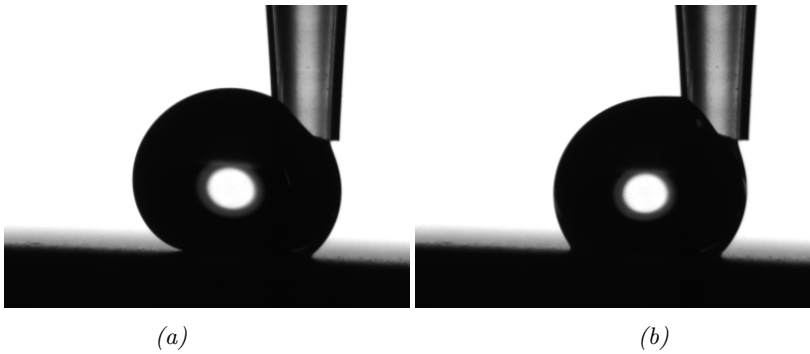


Figure 4.9: The figure shows the ascending (a) and the receding angle (b) of the droplet during measurement on the VD-S-sample. The ascending angle was measured to 168° , and the receding angle 131° .

Table 4.5: The hysteresis values of the vapour deposited samples. Due to the high values measured, additional measurements for each sample were not performed. The values are rounded to the nearest integer.

Sample	U	VD-U	VD-S	VD-N	VD-SN
Ascending Contact Angle	115	156	168	176	173
Receding Contact Angle	47 ²	93	131	107	93
Hysteresis	68	63	37	69	80 ³

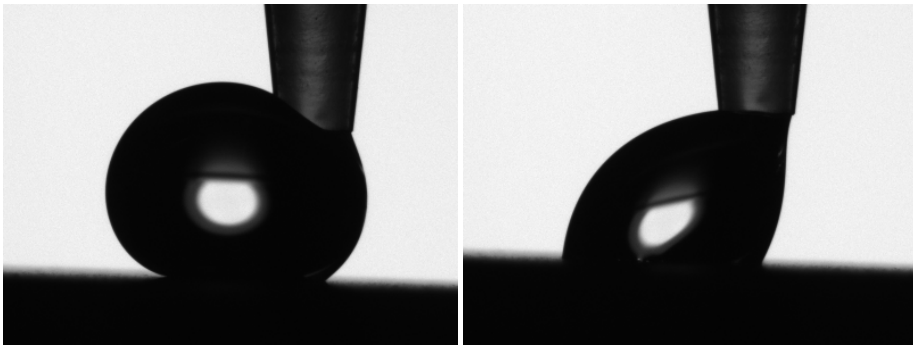
An interesting observation upon measuring the VD-SN-sample was that initially the adhesion between the droplet and the surface was too low for the droplet to wet the surface, and the droplet simply remained adhered to the tip of the pipette upon retraction. This can be seen in Figure 4.10. When forcing the droplet down on the surface by lowering the pipette even more, the droplet seemed to adhere more strongly than usual, leading to the hysteresis measurement shown in Figure 4.11.

²The pipette lost contact with the droplet, due to the extraction of too much water before a change in contact area was observed. The real receding contact angle is likely to be even lower.

³The high hysteresis value of 80° was measured upon forcing the droplet onto the surface, after the initial repelling shown in Figure 4.10.



Figure 4.10: When initially depositing a droplet onto the VD-SN-surface, the droplet seemed to adhere with significantly less force, causing the droplet to be dragged up again by the tip of the pipette.



(a)

(b)

Figure 4.11: Upon forcing the droplet down on the surface of the VD-SN-sample, the droplet would adhere strongly. The ascending angle was measured to 173° , and the receding angle 93° . The hysteresis was thus measured to be 80° .

4.4 Icing Behaviour

As for the hysteresis measurements, only the vapour deposited samples were tested regarding the icing properties. An as-delivered steel sample (U) was also tested in order to easier compare the results obtained from the treated samples.

Single Droplet

The results of how a single droplet behaves when come in contact with each of the cooled surfaces are shown in Figure 4.12. Note that for both the U- and VD-U-samples the droplet adhered to the surface, and did not roll off. For the three remaining samples, the droplet would simply bounce off, leaving the surfaces unaffected.

Spraying and Deicing

When the supercooled water was sprayed on the samples, the water froze as depicted in the first row in Figure 4.13. No change between the samples immediately

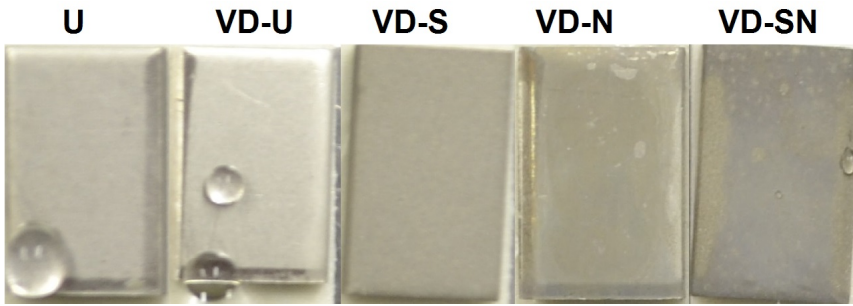


Figure 4.12: A single, supercooled droplet was deposited on each sample. The droplet only adhered on the surfaces of the U and VD-U samples. On the remaining samples, the droplets would simply bounce off, leaving the surface completely dry. Note the small droplet on the right side of the VD-SN-sample. This droplet is a part of the bigger droplet deposited during the experiment, and bounced off the centre of the sample. The area on which it adhered is the area the sample holder was in contact with the sample during nanowire-synthesis, thus no nanowires are present here.

after water-spraying and five minutes after was observed. When comparing the samples, one can see that all have accumulated a uniform layer of ice, except the VD-N-sample, on which some areas are completely without ice. It is difficult to see from the pictures, but the ice accumulated on the VD-N and VD-SN samples is thicker on the bottom half than above. This is not the case for the other three samples.

The samples were moved out of the freezer and into room temperature where the deicing of the samples was observed. For all samples except the VD-SN, the ice would steadily melt, and the water slide off of the samples. After 6 minutes, these samples were all dry. For the VD-SN-sample, the ice would melt in the same degree as for the other samples, but the water would not slide off but rather adhere to the surface, leaving the sample completely wet.

Also, please note the small droplet on the unblasted sample with ZnO-NWs, which is more closely depicted in Figure 4.14. This small droplet is visible during the whole experiment, depicted in Figure 4.13. This droplet never froze, even after 5 minutes in the freezer, even though the rest of the water froze on impact. The droplet also remained adhered to the surface throughout the deicing test, even though the melted ice slid off.

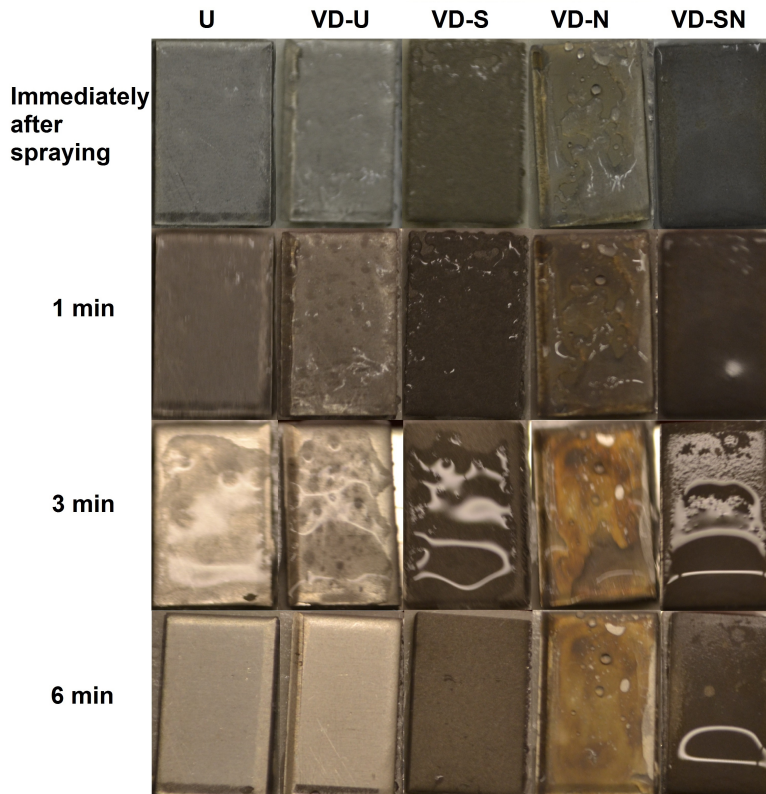


Figure 4.13: Anti-icing and deicing results of the vapour deposited samples. The pictures are taken immediately after spraying in the freezer, and after 1, 3 and 6 minutes of deicing in room temperature.

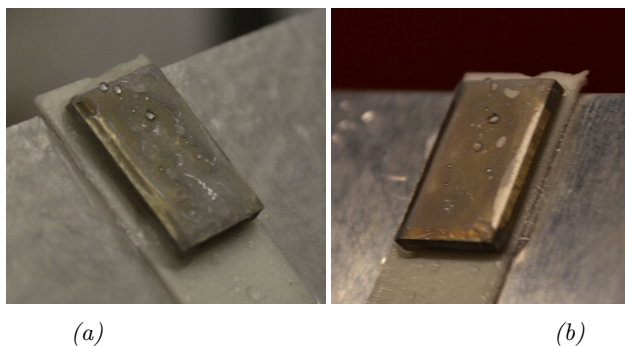


Figure 4.14: A small unfrozen droplet is visible on the VD-N-sample during the anti-icing experiment. No sign of freezing was observed after (a) 5 minutes in the freezer. Furthermore, no change was observed when the samples was moved out in (b) room temperature.

Chapter 5

Discussion

5.1 Surface Treatments Pre-Coating

Sand blasting and hydrothermal synthesis of ZnO-NWs were chosen for the development of micrometric- and nanometric roughness, respectively. Sand blasting was chosen mainly because it is a cheap, effective, and simple method with high reproducibility. This method was also used in previous work by the author, and showed promising results. The hydrothermally synthesised ZnO-NWs were chosen due to the broad range of substrates on which they could be grown with the use of few and inexpensive chemicals. Work performed by Guo et al. [50] and He et al. [49], to mention some, have shown ZnO-NWs to have potential for hydrophobic applications, even at sub-zero temperatures. Guo did also work on steel, but the micrometric roughness was introduced by a more controlled method of creating a ratchet-structure with a periodicity of 300 μm . This method is both more time consuming and more expensive compared to sand blasting used in this thesis. The combination of sand blasting and ZnO-NWs is an approach the author has not found similar in literature.

5.1.1 Sand Blasting

Compared to literature, e.g. Beckford and Zou [21] who achieved a contact angle of 157° on a sand blasted sample with a R_a -value of 1532 nm, the achieved R_a -value of 1600 nm, given in Table 4.1, is satisfactory for achieving superhydrophobic contact angles. It is believed that by the application of even finer sand particles, the roughness would be even more desirable for hydrophobic purposes. However, according to Figure 2.8 the peak-to-peak distance achieved is already well within the range of Cassie-Baxter wetting state. Improved roughness will therefore not necessarily result in a significant increase of contact angle values, given that the desired wetting state may already be achieved. It must however be noted that the peak-to-peak distances on a sand blasted sample are randomly distributed. In Figure 4.2 the distance between the two first peaks of significant height is around 250 μm , whereas the distance to the subsequent peak is below 50 μm . A full

Cassie-Baxter wetting over the whole sample can thus not be expected, but rather a combination of different wetting states. Given this, some positive difference should be visible when using finer sand particles. The sand particles with a diameter of 150 μm were used as they were the finest available.

5.1.2 ZnO-Nanowire Synthesis

Several papers regarding the ZnO-NW synthesis through the hydrothermal method report the broad range of substrates on which it can be applied. However, the papers also stress the need for the substrates to be flat. The results when grown on sand blasted samples were therefore initially unknown.

The parameters play an important role on the dimensions of the ZnO-NWs. Even though the same parameters as in literature were used in this thesis, ZnO-NWs with different dimensions were the result. The parameters used in this thesis are therefore a product of adaption from literature and adjustments through trial-and-error.

An interesting observation of the NWs on the N- and SN-samples was that the dimensions were slightly changed to the worse when synthesised on a sand blasted surface rather than a smooth one. The height and density were lowered, and the diameter grew. All these changes may result in a less desirable behaviour regarding both hydrophobicity and icephobicity, as explained regarding height of the nanowires on hydrophobicity, in Figure 2.8, and diameter on icephobicity, Figure 2.9. The reasons for this negative difference in growth behaviour is unknown, but is likely to be due to the uneven surface, as literature readily express the need for smooth surfaces. Upon further trial-and-error, adjustments of the parameters to achieve more desirable dimensions should be possible.

5.2 Deposition

The precursor and sol-recipe were chosen mainly due to being familiar through the work performed by former master students Halvorsen and Raasok. The precursor is expensive so for further experiments or application in larger scales, a substitute may be desired as there are several options available.

5.2.1 Dip-Coating

In order to use dip-coating as the depositing method, a sol has to be synthesised. As the thickness of the deposited layer is proportional to the viscosity of the sol, a volatile sol would be desirable in order to avoid compromising the micrometric- and nanometric roughness induced. As this thesis is a continuation of the theses written by Halvorsen and Raasok, the more volatile of their sol-recipes was chosen, having a viscosity comparable to water, given in Table 4.2. Note that this sol has a pH of 10. As explained using Figure 2.25, an alkaline sol will contain small particles along with being thicker compared to an acidic sol with the same initial

viscosity. The small particles present in the sol are shown in the SEM-images in Figure 4.5. As we will see when discussing the results from the contact angle measurements, these small particles may have had an impact. It is advisable upon further research to use an acidic sol in order to avoid compromising the topography more than necessary. To minimise potential sources of error even further, the full elimination of dip-coating for the benefit of vapour deposition may be even more desirable.

5.2.2 Vapour Deposition

Due to the sources of error regarding dip-coating, being the small particles in the sol and the thickness of the deposited layer, the effect of changing method of deposition was investigated. By using vapour deposition one would be certain to be able to coat even within the small grooves with a thin, homogeneous coating-layer, without compromising the roughness. No sol was needed for this method to be performed.

When coating, no visible signs of the coating on the samples were present, in contrast to the dip-coating where the dipped end would be slightly darkened. This led to the belief that the structure on the surface of the samples was more or less unchanged after vapour deposition, whereas the dip-coating may have affected the structure. This is clearly visible in the SEM-images taken of the two surfaces, shown in Figure 4.6.

Even though errors regarding particles in the sol and compromising the roughness are excluded with the use of vapour deposition, the uncertainty of the binding of the molecules remains, as described in Section 2.5.2. No effort has been made during this thesis to determine the alignment of the molecules and as will be seen when addressing the hysteresis values, potential misalignments may have had a significant negative impact.

5.2.3 The Importance of Ethanol-Rinsing

The deposition methods were always finalised with a washing step, where the samples were rinsed with ethanol from a wash-bottle. This was proven to be of high importance as the contact angle values were significantly improved by this simple treatment, as shown for the VD-N-sample in Figure 4.7. When coating the substrates, the hydrophobic molecules should preferably be aligned so that the hydrophobic groups, i.e. the fluorine, points upwards from the surface, as depicted in Figure 2.31. Let us assume, for this hypothesis, that the first layer of molecules have thoroughly coated the surface with correct alignments. Now, new molecules will come in contact with the coated surface, and interact through van-der-Waal bonds. These bonds have no preferred orientation, meaning the molecules will be randomly oriented on the surface. Some ethyl-groups will in this case be facing upwards, available for water droplets to wet, causing high adherence due to their hydrophilicity. After the finalising heat-treatment, covalent bonds will be created between the surface and the first layer of molecules. The abundant molecules will however still adhere through van-der-Waals bonds. By subsequently rinsing the

surface with ethanol, these weakly bonded molecules will be solved, leaving the surface with only correctly aligned molecules present. The hypothesis described here seems plausible, as the surfaces experience an increase in hydrophobicity after ethanol rinsing.

5.3 Wetting

Contact angle results

As expected, Table 4.4 shows an increase in contact angle values from untreated samples to mono-layer roughness, and further to hierarchical roughness.

U-samples

When looking at Table 4.4 the first thing one may notice is that the contact angles of the coated U-samples have a value above that of the theoretical maximum for smooth surfaces, 120° . It is here important to point out that the untreated steel samples are not indeed entirely smooth. Steel consists of several small grains, and between each grain there are grain boundaries. On the surface of the steel these grain boundaries are visible due to their appearance as small valleys, visible in Figure 4.1. Although the roughness of such surfaces are not anywhere near the roughness of sand blasted surfaces, one would expect a slight increase of contact angle compared to a perfectly smooth surface.

In addition, an alkaline sol has in this thesis been used when dip-coating, which as explained in Section 5.2.1 contain small particles, pictured in Figure 4.5. These particles will be randomly distributed on the surface and add roughness. The combination of these two roughness-increasing factors will thus give a higher increase in contact angle than only the grain boundaries will, explaining why the DC-U-sample have a higher contact angle than VD-U-sample.

S-samples

When micrometric roughness is induced, as shown in Figure 4.2, the contact angle value increases significantly and superhydrophobic values are achieved. Here the difference between dip-coating and vapour deposition is significantly smaller than for the U-samples. The slight difference can be explained through a small roughness-addition from the sol-particles, or simply ignored as the difference is within the standard deviation value. As mentioned, the peak-to-peak distances measured on these samples are mostly within the range of Cassie-Baxter wetting, and thus high contact angle values and relatively low hysteresis values should be expected.

N-samples

When nanometric roughness is introduced, as on the N-samples shown in Figure 4.3, dip-coating is no longer an applicable method. A difference of approximately 7°

is a value that cannot be ignored, especially above the limit of superhydrophobicity where a degree up or down may have significant consequences. The reasons for the large difference is easy to pinpoint when looking at the surface after coating on Figure 4.6. Although the pictures are somewhat distorted by the coating being sensitive to the electrons from the SEM, one can see a difference between the two pictures whose structure should be the same. On the dip-coated sample, Figure 4.6(a), the thickness of the coating is too large, resulting in a smoother surface where the single ZnO-NWs are no longer sharply visible. On Figure 4.6(b) one can easily distinguish one NW from another, thus leaving the nanometric roughness uncompromised.

SN-samples

Taking the latter paragraph into consideration, it is no surprise that the SN-samples, shown in Figure 4.4, show a significant increase in contact angle values when vapour deposition is used. The VD-SN-sample shows a consistent contact angle of approximately of 164° . This is a high contact angle value. Remember the contact angle achieved through the use of femtosecond laser mentioned in Section 2.3.2, measured to 158° which showed very good superhydrophobic behaviour.

Hysteresis Results

Hysteresis values along with receding contact angle values are likely the most important parameters when introducing icephobicity through hydrophobicity. Further, in order to achieve superhydrophobicity the hysteresis value needs to be less than 10° , by definition. This was not achieved in this thesis, as all samples showed adhesive behaviour as in Figure 4.8. The achieved hysteresis- and receding contact angle values are visible in Table 4.5. The best results, 37° , were measured on the VD-S-sample, shown in Figure 4.9. However, as mentioned with regards to Figure 4.10, the VD-SN-sample showed a brief moment of desired behaviour when the droplet would not wet the surface, but rather remain in contact with the needle. Upon forcing the droplet down on the sample, the droplet adhered more strongly than all other samples, visible in Figure 4.11. The hysteresis on this sample was measured to 80° .

There are several possible reasons for why the hysteresis values are high. First, the less likely hypotheses will be addressed, before the more likely ones are addressed.

As described in the theory section, inhomogeneity may be the reason for some hysteresis. For example, the nanometric roughness may have different dimensions on different areas on the sample. This is not likely to solely explain the hysteresis, due to the high hysteresis also present on the VD-U-sample. It can however contribute to the high value in some degree.

The sample itself, without the presence of coating, is either slightly hydrophilic or have a contact angle of approximately 90° , as given in Table 4.4. Given the chance that after deposition bare areas would be left behind, causing water to adhere to the bare steel, one could believe this to be the reason for the high hysteresis. Vapour

deposition over a period of 22 hours is however a long time, and will most likely yield a thorough and homogeneous coating layer.

Addressing the state with which the water wets the surface may be of more interest. According to Figure 2.8, the peak-to-peak distance of the micrometric roughness should be within the area of Cassie-Baxter wetting state, meaning it should exhibit a higher receding contact angle than an equivalent smooth surface, as explained in Section 2.1.2. The equivalent smooth surface would in this case be the VD-U-sample. This behaviour is observed for the VD-S-sample. On the samples with ZnO-NWs the same is not observed. For the VD-N- and VD-SN-samples the hysteresis value is higher than for the VD-U-sample. This leads us to believe that the wetting behaviour is not full Cassie-Baxter, rather a combined state, or even full Wenzel for the VD-SN sample. Upon forcing the droplet down in the surface, after it initially refused, as shown in Figure 4.10, the droplet might have undergone a Cassie-Baxter to Wenzel transition. This transition would result in a significant increase of adhesion, and result in lower receding contact angle- and higher hysteresis values than on the equivalent smooth surface.

The VD-N-sample did not exhibit the same high hysteresis value as the VD-SN-sample, most likely due to the droplet not needing to be forced down onto the sample. The hysteresis values were however still high. This might be also be explained by the wetting. Since the droplet did not need to be forced in the same manner, the wetting state is likely to be a combined one; partly Cassie-Baxter and partly Wenzel. The reason for why full Cassie-Baxter is not achieved might lie in the dimensions of the developed ZnO-NWs. The dimensions of each NW, and especially the density achieved in this thesis is not as desirable as in literature. The distance between each NW could increase the chance of wetting between them, causing a larger contact area and larger hysteresis values. Notice also that the dimensions of the ZnO-NWs developed on the sand blasted surfaces compared to smooth surfaces are less desirable. This small change could also be a contributing factor for the higher hysteresis noticed on the VD-SN-sample.

In addition to both the state of wetting and the dimensions of the ZnO-NWs, there is the alignment of the hydrophobic molecules on the surface. As explained, the peak-to-peak distance of the micrometric roughness should be within the area of Cassie-Baxter wetting, and probably (mainly) is which would explain why the VD-S-sample shows the lowest hysteresis value. This value is however still too high. No effort has in this thesis been made to investigate the orientation of the molecules deposited, meaning that the molecules could be bonded by one or three ethyl-groups, as mentioned in Section 2.5.2. If indeed the molecules bond with less than three OH-groups on the surface, the droplet would increase the adhesion with the surface, since the ethyl-groups are hydrophilic, which would explain the high hysteresis on the VD-U-sample. This would of course be a contributing factor for all other coated samples as well.

5.4 Anti-Icing Results

The results from the spraying test will be addressed first. Due to the high hysteresis measured earlier, it was expected that the water would indeed be able to crystallise and adhere to the surface, which proved right. There are however slight differences in how the water crystallised. On the three substrates U, VD-U, and VD-S the water would crystallise somewhat homogeneously, creating a layer of ice with approximately the same thickness over the whole substrate. When examining the two surfaces where ZnO-NWs had been synthesised, the thickness was observed to be greater on the lower part of the samples. This may be due to the increased hydrophobicity, compared to the other samples, and the water would thus experience some hydrophobic interaction when come in contact with the substrate, resulting in the water moving downwards before finally crystallising. Also, note that all samples are completely covered in ice, except the VD-N-sample. That this sample only should be able to repel supercooled water is not likely, as the hysteresis value for the sample is high. It must here be noted that the nature of the experiment is highly dependent on the person performing it. The samples are all manually sprayed two times with a spray bottle. To achieve the exact same spraying behaviour from the exact same distance on all samples is difficult, and thus small differences in ice accumulation may occur. The need for a better, more reproducible icing test would be of high interest. When that is said, Figure 4.14 shows an interesting observation. Here a small droplet on the VD-N-sample is depicted. This droplet did not experience crystallisation even after 5 minutes in the freezer. This droplet may thus have wetted the surface with the desired Cassie-Baxter state, minimising the contact area and thus the heat-transfer and nucleation. The high hysteresis prevented the droplet from sliding off.

The deicing of the samples showed an interesting observation. The ice on all samples seemed to melt with approximately the same speed, however, the water behaved differently on the VD-SN-sample. On the four other samples, the water simply slid off, leaving the sample completely dry. On the VD-SN-sample however, the water seemed to adhere strongly, resulting in the sample remaining almost completely wet even after 6 minutes. Please note, on Figure 4.13, that the only part of the sample that is not wet after 6 minutes, is the part where no ZnO-NWs had been created. These areas are due to the sample holder, depicted in Figure 3.4. It seems thus that the ZnO-NWs increase the adherence of water on the surface, and instead of the Lotus effect, we achieve Petal-like behaviour. The reason the same behaviour is not observed on the VD-N-sample is uncertain. However, remember that the dimensions and density ZnO-NWs developed on sand blasted surfaces are less desirable than on smooth surfaces. This small difference in topography could have a significant effect on the wetting behaviour, as shown in Figure 2.8, where a small difference could result in Petal-like behaviour instead of Lotus.

Single Droplet Test

Some anti-icing behaviour was observed during the test with single droplets, which results are shown in Figure 4.12. Here the droplet adhered and froze only on the U-

and VD-U-samples, and the rest showed a bounce-off behaviour, leaving the surface completely dry. This seems to be in coherence with what was experienced when depositing single droplets on the VD-SN-samples for contact angle measurements, Figure 4.10. When the droplet first comes in contact with the surface, it is initially repelled and will not adhere strongly. However, when forced onto the surface, the droplet seems to settle and adhere with a greater force than initially. It seems that the same happens during the icing tests. When a single droplet with speed comes in contact with an inclined surface it does not have time to settle, and is repelled due to the initial hydrophobic behaviour of the surface. When hitting the surface with higher kinetic energy through spraying, the droplets come in contact with the surface more powerfully, resulting in instantaneous full wetting, and the droplets settle and adhere strongly, especially on the VD-SN-sample with the least favourable nano-structure.

5.5 Summary of Discussion

Summarising the discussion, one can safely conclude that dip-coating is not a precise enough method to coat a surface with nanometric roughness, as the ZnO-nanowires in this thesis. Vapour deposition ensures a homogeneous and thin coating layer, and preserves the nanometric roughness which is of high importance for the hydrophobic and icephobic behaviour.

Although the vapour deposition is better, it is not perfect. The high hysteresis observed on all coated samples gives indications that the hydrophobic ends of the molecules are not perpendicularly aligned, leaving the hydrophilic end available for the water to come in contact with. This is something that has to be investigated.

As explained during the theory section, the dimensional differences are small between surfaces showing the Lotus-effect and those showing the Petal-effect. The nano-structures developed in this thesis are not as desirable as found in literature, and may result in a less desirable wetting state, leading to high adhesive forces. The ZnO-NWs developed on sand blasted surfaces shows even less desirable dimensions, and may be the reason for the difference between the VD-N- and VD-SN-samples.

Chapter 6

Conclusion

In this thesis an effort has been made to further the understanding of the link between topography, hydrophobicity and icing behaviour. The topography of steel samples have been made by mimicking the hierarchical topography of Lotus leaves found in nature. The micrometric roughness is introduced through sand blasting, and the nanometric through the synthesis of ZnO-nanowires. The surfaces were subsequently coated by a highly hydrophobic fluorosilane with the use of dip-coating and vapour deposition.

The sol-recipe used during the dip-coating process was supplied through the work of former master students, and resulted in a thick coating layer that compromised the nanometric roughness from the nanowires. The vapour deposition had no such negative effect on the roughness, and is regarded as a superior method for this purpose. This superiority was also visible in the contact angle values. By treating the surfaces with ZnO-nanowires with the vapour deposition, the contact angles rose with a value of 6-7 °. A contact angle of 164 ° was achieved on the hierarchical sample.

Even though such high contact angles were achieved, the hysteresis values registered were unsatisfactory. The lowest hysteresis value measured was on the sand blasted sample with 37°, whereas the hierarchical sample with the high contact angle showed a hysteresis value of 80°. In order to repel icing the hysteresis measurements should ideally be close to zero, or at least $< 10^\circ$ to achieve superhydrophobic behaviour by definition.

During the spray-icing experiment no sample showed definite anti-icing behaviour as water crystallised on all samples. The samples with ZnO-nanowires did however show small hints of water repulsion prior to crystallisation. Upon subsequent melting all samples were completely dry within 6 minutes, except the hierarchical sample. Even though the ice melted in the same degree as for the other samples, the water seemed to adhere strongly and did not slide off, leaving the sample completely wet.

The high hysteresis values and the undesired deicing behaviour of the hierarchical

sample is believed to be a combination of two factors; the dimensions of the ZnO-nanowires and the coating layer. The dimensions and densities of the nanowires achieved in this thesis are not as desirable as in literature. It is thus believed that the wetting is not full Cassie-Baxter, and upon further influence it will undergo a transition to full Wenzel. Since relatively large hysteresis values are also experienced on the samples with no nanowires present, it is also believed that the hydrophobic molecules on the surface are not perpendicularly aligned, causing hydrophilic ethyl-groups to be available for contact with the water droplets.

Improvement of the dimensions and densities of the ZnO-nanowires has to be performed in order to achieve full Cassie-Baxter wetting, and resist subsequent transition to the Wenzel state. Furthermore, investigation regarding the alignment of the surface molecules has to be performed.

Chapter 7

Further Work

There is still much research to be performed within the field of icephobicity before such behaviour can be utilized in industry. Even though the interest of this field has grown significantly the last years, it still faces big challenges such as Cassie-Baxter to Wenzel transition at low temperatures, the mechanical properties of the surfaces, and up-scaling.

The use of ZnO-NWs on sand blasted steel samples have in this thesis shown great potential, with contact angles as high as 164° . The hysteresis problem is however something that has to be overcome. For a continuation of this work, the further improvement of the ZnO-NW dimensions and densities is a good starting point. By increasing the density and height, and decreasing the diameter to values found in literature, the hysteresis values may be significantly reduced. Note that the dimensions and densities achieved in this thesis are different for smooth and sand blasted surfaces. Extensive adjustments of parameters to achieve desirable results on rough substrates may thus be needed.

The hypothesis made in this thesis regarding the alignment of the hydrophobic molecules is something that has to be verified or disproved. If the hypothesis is verified, both the contact angle- and especially the hysteresis values may experience a significant improvement by aligning the molecules. However, if the hypothesis is disproved the thoroughness of the deposition method must be addressed. If the water droplets come in contact with free OH-groups on the steel surface, this may be the reason for the strong adhesion.

Lastly, the mechanical properties of the ZnO-NWs and the coating layer may be beneficial to examine. With poor mechanical properties a surface will have to be continuously maintained to preserve the desired properties, resulting in a lasting need of manpower and funds, no different than the constant need of deicing. Even if ZnO-NWs show poor mechanical properties, they can still be used in research to further the understanding of the link between topography, hydrophobicity and icing behaviour, as they are relatively easy synthesised, with easily adjustable parameters.

Bibliography

- [1] Ytkemiska institutet, Institute for surface chemistry, “Nanotechnology to avoid problems with ice.” Available: <http://www.yki.se/en/media/news/sidor/101008.aspx> [Accessed 11th of December 2014].
- [2] United States Environmental Protection Agency, “Environmental impact and benefit assessment for proposed effluent limitation guidelines and standards for the airport deicing category,” July 2009. Available: http://water.epa.gov/scitech/wastetech/guide/airport/upload/2009_08_28_guide_airport_Airport_EIB_Proposed_2009.pdf [Accessed 18th of March 2015].
- [3] Privatefly.com, “De-icing for private jets.” Available: <http://www.privatefly.com/privatejet-services/de-icing-private-jets.html> [Accessed 11th of December 2014].
- [4] B. Borrell, “How does ice cause a plane to crash?,” February 2009. Available: <http://www.scientificamerican.com/article/ice-flight-3407/> [Accessed 21st of April 2015].
- [5] J. Fallows, “About the terrible small-plane crash over I-287 in new jersey,” December 2011. Available: <http://www.theatlantic.com/national/archive/2011/12/about-the-terrible-small-plane-crash-over-i-287-in-new-jersey/250348/> [Accessed 21st of April 2015].
- [6] Teknisk Ukeblad, “Her spyler helikopteret bort et tykt lag med is,” February 2015. Available: <http://www.tu.no/kraft/2015/02/01/her-spyler-helikopteret-bort-et-tykt-lag-med-is> [Accessed 2nd of February 2015].
- [7] E. Jenssen, “Sea spray icing,” May 2011. Available: http://www.unis.no/60_NEWS/6070_Archive_2011/n_11_05_24_ice/sea_spray_icing_news_24052011.htm [Accessed 18th of March 2015].
- [8] S. M. Hanetho, *Hybrid Aminopropyl Silane-based Coatings on Steel*. Phd thesis, NTNU, 2012.

-
- [9] A. M. Halvorsen, “Hydrophobic coatings for anti-icing application,” master’s thesis, NTNU, 2014.
- [10] E.-K. Raasok, “Hydrophobic coatings for anti-icing application,” master’s thesis, NTNU, June 2014.
- [11] O.-B. E. Moe, “Hydrophobic surfaces for anti-icing applications.” December 2014.
- [12] C. Antonini, M. Innocenti, T. Horn, M. Marengo, and A. Amirfazli, “Understanding the effect of superhydrophobic coatings on energy reduction in anti-icing systems,” *Cold Regions Science and Technology*, vol. 67, pp. 58–67, 2011.
- [13] C. Yang, U. Tartaglino, and B. N. J. Persson, “Influence of surface roughness on superhydrophobicity,” *Physical Review Letters*, vol. 97, no. 116103, p. 4, 2006.
- [14] M. A. Frank, A. R. Boccaccini, and S. Virtanen, “A facile and scalable method to produce superhydrophobic stainless steel surface,” *Applied Surface Science*, vol. 311, pp. 753–757, 2014.
- [15] Ramé-Hart Instrument Co., “Glossary of surface science terms.” Available: <http://www.ramehart.com/glossary.htm> [Accessed 19th of March 2015].
- [16] H. J. Ensikat, P. Ditsche-Kuru, C. Neinhuis, and B. W., “Superhydrophobicity in perfection: the outstanding properties of the lotus leaf,” *Beilstein Journal of Nanotechnology*, vol. 2, pp. 152–161, 2011.
- [17] D. Quere, “Non-sticking drops,” *Reports on Progress in Physics*, vol. 68, pp. 2495–2532, 2005.
- [18] B. Dumé, “Turning the lotus leaf on its head,” April 2005. Available: <http://nanotechweb.org/cws/article/tech/21936> [Accessed 18th of March 2015].
- [19] Nanostart AG, “Nano:start newsletter.” Available: <http://www.nanostart.de/en/news/newsletter/archive/view/listid-6-nanostart-news-english/mailid-321-newsletter-march-vitae-dr-christoph-weiss-new-web-presences-microlight-and-nanosys-nanowebtalk-pre-interview-and-retrospective-nanotech-for-surfaces> [Accessed 19th of March 2015].
- [20] R. N. Wenzel, “Resistance of solid surfaces to wetting by water,” *Industrial and Engineering Chemistry*, vol. 28, pp. 988–994, August 1936.
- [21] S. Beckford and M. Zou, “Micro/nano engineering on stainless steel substrates to produce superhydrophobic surfaces,” *Thin Solid Films*, vol. 520, pp. 1520–1524, 2011.

- [22] R. J. Vrancken, H. Kusumaatmaja, K. Hermans, A. M. Prenen, O. Pierre-Louis, C. W. M. Bastiaansen, and D. J. Broer, "Fully reversible transition from wenzel to cassie-baxter states on corrugated superhydrophobic surfaces," *Langmuir*, vol. 26, no. 5, pp. 3335–3341, 2010.
- [23] F. Xia and L. Jiang, "Bio-inspired, smart, multiscale interfacial materials," *Advanced Materials*, vol. 20, pp. 2842–2858, 2008.
- [24] A. J. Meuler, G. H. McKinley, and R. E. Cohen, "Exploiting topographical texture to impart icephobicity," *ACSnano: Perspective*, vol. 4, no. 12, pp. 7048–7052, 2010.
- [25] Biolin Scientific, "Hysteresis," 2014. Available: <http://www.biolinscientific.com/application/hysteresis-phenomenon/> [Accessed 29th of November 2014].
- [26] Y. L. Chen, C. A. Helm, and J. N. Israelachvili, "Molecular mechanisms associated with adhesion and contact angle hysteresis of monolayer surfaces," *The Journal of Physical Chemistry*, vol. 95, pp. 10736–10747, 1991.
- [27] B. Bhushan and M. Nosonovsky, "The rose petal effect and the modes of superhydrophobicity," *Philosophical Transactions of the Royal Society A*, vol. 368, pp. 4713–4728, 2010.
- [28] B. Bhushan and E. K. Her, "Fabrication of superhydrophobic surfaces with high and low adhesion inspired from rose petal," *Langmuir*, vol. 26, no. 11, pp. 8207–8217, 2010.
- [29] F. D. Nicola, P. Castrucci, M. Scarselli, F. Nanni, I. Cacciotti, and M. D. Crescenzi, "Super-hydrophobic multi-walled carbon nanotube coatings for stainless steel," *Nanotechnology*, vol. 26, no. 145701, 2015.
- [30] W. Barthlott, T. Schimmel, S. Wiersch, K. Koch, M. Brede, M. Barczewski, S. Walheim, A. Weis, A. Kaltenmaier, A. Leder, and H. F. Bohn, "The salvinia paradox: Superhydrophobic surfaces with hydrophilic pins for air retention under water," *Advanced Materials*, vol. 22, no. 21, pp. 2325–2328, 2010.
- [31] W. Barthlott, T. Schimmel, S. Wiersch, K. Koch, M. Brede, M. Barczewski, S. Walheim, A. Weis, A. Kaltenmaier, A. Leder, and H. F. Bohn, "From plants to ship coatings: Air retaining surfaces for drag reduction." Available: http://www.lotus-salvinia.de/pdf/Flyer_Hannover_BIOKON_14_Eng_Final.pdf [Accessed 31st of May 2015].
- [32] L. Feng, Y. Zhang, J. Xi, Y. Zhu, N. Wang, F. Xia, and L. Jiang, "Petal effect: A superhydrophobic state with high adhesive force," *Langmuir*, vol. 24, pp. 4114–4119, 2008.

- [33] S. A. Kulinich and M. Farzaneh, "Alkylsilane self-assembled monolayers: modeling their wetting characteristics," *Applied Surface Science*, vol. 230, pp. 232–240, 2004.
- [34] V. Hejazi, *Wetting, Superhydrophobicity, and Icephobicity in Biomimetic Composite Materials*. Ph.d.-thesis, University of Wisconsin Milwaukee, May 2014.
- [35] V. Hejazi, K. Sobolev, and M. Nosonovsky, "From superhydrophobicity to icephobicity: forces and interaction analysis," *Scientific Reports*, 2013.
- [36] L. Cao, A. K. Jones, V. K. Sikka, J. Wu, and D. Gao, "Anti-icing superhydrophobic coatings," *Langmuir*, vol. 25, no. 21, pp. 12444–12448, 2009.
- [37] S. Farhadi, M. Farzaneh, and S. A. Kulinich, "Anti-icing performance of superhydrophobic surfaces," *Applied Surface Science*, vol. 257, pp. 6264–6269, 2011.
- [38] M. Nosonovsky and V. Hejazi, "Why superhydrophobic surfaces are not always icephobic," *Nano Letters: Perspective*, vol. 6, no. 10, pp. 8488–8491, 2012.
- [39] S. A. Kulinich and M. Farzaneh, "How wetting hysteresis influences the ice adhesion strength on superhydrophobic surfaces," *Langmuir*, vol. 25, no. 16, pp. 8854–8856, 2009.
- [40] A. J. Meuler, D. Smith, K. K. Varanasi, J. M. Mabry, G. H. McKinley, and R. E. Cohen, "Relationships between water wettability and ice adhesion," *Applied Materials & Interfaces*, vol. 2, no. 11, pp. 3100–3110, 2010.
- [41] Biolin Scientific, "Putting tensiometry to work," 2014. Available: <http://www.biolinscientific.com/attension/applications/> [Accessed 13th of April 2015].
- [42] H. Bhadeshia and R. Honeycombe, *Steels: Microstructure and Properties*. Elsevier, third ed., 2006. ISBN: 978-0-7506-8084-4.
- [43] International Stainless Steel Forum, "The stainless steel family." Available: <http://www.worldstainless.org/Files/issf/non-image-files/PDF/TheStainlessSteelFamily.pdf> [Accessed 18th of March 2015].
- [44] British Stainless Steel Association, "Stainless steel grades datasheets." Available: <http://www.bssa.org.uk/topics.php?article=606&featured=1> [Accessed 18th of March 2015].
- [45] Cougartron, "Best passivation method for stainless steel," January 2015. Available: <http://www.cougartron.com/en/blog/best-passivation-method-stainless-steel> [Accessed 8th of April 2015].
- [46] L. Li, V. Breedveld, and D. W. Hess, "Creation of superhydrophobic stainless steel surface by acid treatments and hydrophobic film deposition," *ACS Applied Materials & Interfaces*, vol. 4, pp. 4549–4556, 2012.

- [47] O. Cakir, "Study of etch rate and surface roughness in chemical etching of stainless steel," *Key Engineering Materials*, vol. 364-366, pp. 837-842, 2007.
- [48] K. G. Swift and J. D. Booker, *Manufacturing Process Selection Handbook*, ch. 9. Surface Engineering Processes, pp. 257-260. Elsevier, 2013.
- [49] M. He, J. Wang, H. Li, and Y. Song, "Super-hydrophobic surfaces to condensed micro-droplets at temperatures below the freezing point retard ice/frost formation," *Soft Matter*, vol. 7, pp. 3993-4000, 2011.
- [50] P. Guo, Y. Zheng, M. Wen, C. Song, Y. Lin, and L. Jiang, "Icephobic/anti-icing properties of micro/nanostructured surfaces," *Advanced Materials*, vol. 24, pp. 2642-2648, 2012.
- [51] A. Y. Vorobyev and C. Guo, "Multifunctional surfaces produced by femtosecond laser pulses," *Journal of Applied Physics*, vol. 177, no. 033103, p. 5, 2015.
- [52] Y. Zhang, M. K. Ram, E. K. Stefanakos, and D. Y. Goswami, "Synthesis, characterization, and applications of ZnO nanowires," *Journal of Nanomaterials*, vol. 2012, p. 22, 2012.
- [53] L. E. Greene, M. Law, D. H. Tan, M. Montano, J. Goldberger, G. Somorjai, and P. Yang, "General route to vertical ZnO nanowire arrays using textured ZnO seeds," *Nano Letters*, vol. 5, no. 7, pp. 1231-1236, 2005.
- [54] S. H. Ko, D. Lee, N. Hotz, J. Yeo, S. Hong, K. H. Nam, and C. P. Grigoropoulos, "Digital selective growth of ZnO nanowire arrays from inkjet-printed nanoparticle seeds on a flexible substrate," *Langmuir*, vol. 28, pp. 4787-4792, 2012.
- [55] L. E. Greene, M. Law, J. Goldberger, F. Kim, J. C. Johnson, Y. Zhang, R. J. Saykally, and P. Yang, "Low-temperature wafer-scale production of ZnO nanowire arrays," *Angewandte Chemie, International Edition*, vol. 42, pp. 3031-3034, 2003.
- [56] L. Vayssieres, "Growth of arrayed nanorods and nanowire of ZnO from aqueous solutions," *Advanced Materials*, vol. 15, pp. 464-466, March 2003.
- [57] J. B. Shim, H. Chang, and S. Kim, "Rapid hydrothermal synthesis of zinc oxide nanowires by annealing methods on seed layers," *Journal of Nanomaterials*, p. 6, 2011.
- [58] W. Yang, F. Wan, S. Chen, and C. Jiang, "Hydrothermal growth and application of ZnO nanowire films with ZnO and TiO₂ buffer layers in dye-sensitized solar cells," *Nanoscale Res Lett*, vol. 4, pp. 1486-1492, 2009.
- [59] O. Akhavan, M. Mehrabian, K. Mirabbaszadeh, and R. Azimirad, "Hydrothermal synthesis of ZnO nanorod arrays for photocatalytic inactivation of bacteria," *Journal of Physics D: Applied Physics*, vol. 42, p. 10, 2009.

- [60] S. Baruah and J. Dutta, "Effect of seeded substrates on hydrothermally grown ZnO nanorods," *Journal of Sol-Gel Science and Technology*, vol. 50, pp. 456–464, 2009.
- [61] W.-Y. Wu, C.-C. Yeh, and J.-M. T, "Effects of seed layer characteristics on the synthesis of ZnO nanowires," *Journal of the American Ceramic Society*, vol. 92, no. 11, pp. 2718–2723, 2009.
- [62] K. Govender, D. S. Boyle, P. B. Kenway, and P. O'Brien, "Understanding the factors that govern the deposition and morphology of thin films of ZnO from aqueous solution," *Journal of Materials Chemistry*, vol. 14, pp. 2575–2591, 2004.
- [63] M. Ladanov, M. K. Ram, G. Matthews, and A. Kumar, "Structure and opto-electrochemical properties of ZnO nanowires grown on n-Si substrate," *Langmuir*, vol. 27, pp. 9012–9017, 2011.
- [64] H. Ghayour, H. R. Rezaie, S. Mirdamadi, and A. A. Nourbakhsh, "The effect of seed layer thickness on alignment and morphology of ZnO nanorods," *Vacuum*, vol. 86, pp. 101–105, 2011.
- [65] S.-F. Wang, T.-Y. Tseng, Y.-R. Wang, C.-Y. Wang, H.-C. Lu, and W.-L. Shih, "Effects of preparation conditions on the growth of zno nanorod arrays using aqueous solution method," *International Journal of Applied Ceramic Technology*, vol. 5, no. 5, pp. 419–429, 2008.
- [66] S. Xu, C. Lao, B. Weintraub, and Z. L. Wang, "Density-controlled growth of aligned ZnO nanowire arrays by seedless chemical approach on smooth surfaces," *Journal of Materials Research*, vol. 23, no. 8, pp. 2072–2077, 2008.
- [67] A. Sugunan, H. C. Warad, M. Boman, and J. Dutta, "Zinc oxide nanowires in chemical bath on seeded substrates: Role of hexamine," *Journal of Sol-Gel Science and Technology*, vol. 39, pp. 49–56, 2006.
- [68] Z. Yuan, J. Yu, N. Wang, and Y. Jiang, "Well-aligned ZnO nanorod arrays from diameter-controlled growth and their application in inverted polymer solar cell," *Journal of Materials Science: Materials in Electronics*, vol. 22, pp. 1730–1735, 2011.
- [69] S. Baruah and J. Dutta, "pH-dependent growth of zinc oxide nanorods," *Journal of Crystal Growth*, vol. 311, pp. 2549–2554, 2009.
- [70] ZYGO, "Surface measurement: Essential for technology." Available: <http://www.zygo.com/?/met/profilers/surfaceroughnessmeasurement.htm> [Accessed 28th of October 2014].
- [71] ETH Zuerich, "Atomic force microscope," 2012. Available: http://www.ferroic.mat.ethz.ch/research/labs_general/afm [Accessed 13th of December 2014].

- [72] J. D. Wright and N. A. J. M. Sommerdijk, *Sol-Gel Materials: Chemistry and Applications*. CRC Press, 2000. ISBN: 978-9-0569-9326-9.
- [73] C. J. Brinker and G. W. Scherer, *Sol-Gel Science: The Physics and Chemistry of Sol-Gel Processing*. Academic Press, Inc., 1990.
- [74] Sigma-Aldrich, “Tetraethyl orthosilicate,” 2014. Available: <http://www.sigmaaldrich.com/catalog/product/aldrich/131903?lang=en®ion=NO> [Accessed 23rd of November 2014].
- [75] S. Y. Chang and T. A. Ring, “Map of gel times for three phase region tetraethoxysilane, ethanol and water,” *Journal of non-crystalline solids*, vol. 147 & 148, pp. 56–61, 1992.
- [76] Accurion, “Silanization.” Available: <http://accurion.com/nanofilm-silanization> [Accessed 30th of April 2015].
- [77] Harrick Plasma, “Benefits of plasma cleaning,” 2014. Available: <http://harrickplasma.com/applications/plasma-cleaning> [Accessed 14th of May 2015].
- [78] L. E. Scriven, “Physics and applications of dip coating and spin coating,” *Materials Research Society Symposium Proceedings*, vol. 121, pp. 717–729, 1988.
- [79] J. Puetz and M. A. Aegerter, *Sol-Gel Technologies for Glass Producers and Users*, ch. 2.2.1: Dip Coating Techniques, pp. 37–48. Springer, 2004.
- [80] J. M. Chovelon, L. E. Aarch, M. Charbonnier, and M. Romand, “Silanization of stainless steel: Influence of application parameters,” *The Journal of Adhesion*, vol. 50, no. 1, pp. 43–58, 1995.
- [81] C. J. Geankoplis, *Transport Processes and Separation Process Principles*. Prentice Hall, 2009. ISBN: 978-0-1310-1367-4.
- [82] K. L. Choy, “Chemical vapour deposition of coatings,” *Progress in Material Science*, vol. 48, pp. 57–170, 2003.
- [83] VWR, “Etanol analaR normapur acs.” Available: https://no.vwr.com/store/catalog/product.jsp?catalog_number=20821.321 [Accessed 25th of November 2014].
- [84] Sigma-Aldrich, “Zinc nitrate hexahydrate.” Available: <http://www.sigmaaldrich.com/catalog/product/sial/228737?lang=en®ion=NO> [Accessed 19th of March 2015].
- [85] Sigma-Aldrich, “Zinc acetate dihydrate.” Available: <http://www.sigmaaldrich.com/catalog/product/sial/383058?lang=en®ion=NO> [Accessed 19th of March 2015].

- [86] Sigma-Aldrich, “Hexamethylenetetramine.” Available: <http://www.sigmaaldrich.com/catalog/product/sial/h6404?lang=en®ion=NO> [Accessed 19th of March 2015].
- [87] Sigma-Aldrich, “Water,” 2014. Available: <http://www.sigmaaldrich.com/catalog/product/sial/38796?lang=en®ion=NO> [Accessed 24th of November 2014].
- [88] P. M. Rørvik, T. Grande, and M. Einarsrud, “Hierarchical PbTiO₃ nanostructures grown on SrTiO₃ substrates,” *Crystal Growth & Design*, vol. 9, no. 4, pp. 1980–1984, 2009.
- [89] Sigma-Aldrich, “1h,1h,2h,2h-perfluorooctyltriethoxysilane,” 2014. Available: <http://www.sigmaaldrich.com/catalog/product/aldrich/667420?lang=en®ion=NO> [Accessed 23rd of November 2014].
- [90] Sigma-Aldrich, “Ammonium hydroxide solution,” 2014. Available: <http://www.sigmaaldrich.com/catalog/product/sial/320145?lang=en®ion=NO> [Accessed 14th of December 2014].
- [91] S. Gilles, “Chemical modification of silicon surfaces for the application of soft lithography,” *Berichte des Forschungszentrums Julich*, May 2007.
- [92] Engineering Toolbox, “Water - dynamic and kinematic viscosity.” Available: http://www.engineeringtoolbox.com/water-dynamic-kinematic-viscosity-d_596.html [Accessed 6th of June 2015].
- [93] W. L. Switzer, “Density of water.” Available: http://www.ncsu.edu/chemistry/resource/H2Odensity_vp.html [Accessed 21st of April 2015].
- [94] P. Shapley, “Temperature effects on density,” 2011. Available: <http://butane.chem.uiuc.edu/pshapley/GenChem1/L21/2.html> [Accessed 21st of April 2015].

Appendices

A Stoichiometric to Volumetric Calculations

Formulas and information about the reactants used in the sol-gel processing needed to calculate the volumetric- from stoichiometric amount are given below.

Table A1: Molar weight and density of β -silane, ethanol, and deionized-water. The information is extracted from [83, 87, 89, 93, 94].

Substance	Molar weight [g/mol]	Density at 25°C [g/mL]
β -silane	510.36	1.3299
Ethanol	46.07	0.7852
DI water (pH adjusted) ¹	18.02	0.9970

$$V = \frac{m}{\rho} \quad (7.1)$$

$$m = n \cdot M \quad (7.2)$$

where V is volume, ρ is density, m is mass, M is the molar weight and n is the number of mol.

¹The effect on molar weight and density from the addition of NH_4OH is neglected, as the amounts added in order to achieve the desired pH-value is insignificant.